Hydrodynamic Shrinkage of Liquid CO_2 Taylor Drops in a Straight Microchannel

Ning Qin, John Z. Wen, and Carolyn L. Ren

Department of Mechanical and Mechatronics Engineering, University of Waterloo, Waterloo, Ontario, Canada N2L3G1
(Received xx xxxxx 2017; revised xx xxxxx 2018; accepted xx xxxxx 2018)

Hydrodynamic shrinkage of liquid CO_2 drops in water under a Taylor flow regime is studied using a straight microchannel (length/width ~ 100). A general form of a mathematical model of the solvent-side mass transfer coefficient (k_s) is developed first. Based on formulations of the surface area (A) and the volume (V) of a general Taylor drop in a rectangular microchannel, a specific form of k_s is derived. Drop length and speed are experimentally measured at three specified positions of the straight channel, namely, immediately after drop generation (position 1), the midpoint of the channel (position 2) and the end of the channel (position 3). The reductions of drop length (L_x, x = 1, 2, 3) from position 1 to 2 and down to 3 are used to quantify the drop shrinkage. Using the specific model, k_s is calculated mainly based on L_x and drop flowing time (t). Results show that smaller CO_2 drops produced by lower flow rate ratios (Q_{LCO2}/Q_{H2O}) are generally characterized by higher (nearly three times) k_s and Sherwood numbers than those produced by higher Q_{LCO2}/Q_{H2O}, which is essentially attributed to the larger effective portion of the smaller drop contributing in the mass transfer under same levels of the flowing time and the surface-to-volume ratio (~ $10^4 \, m^{-1}$) of all drops. Based on calculated pressure drops of the segmented flow in microchannel, the Peng-Robinson equation of state (EOS) and initial pressures of drops at the T-junction in experiments, overall pressure drop (ΔP_t) in the straight channel as well as the resulted drop volume change are quantified. ΔP_t from position 1 to 3 is by average 3.175 kPa with a ~1.6% standard error, which only leads to relative drop volume changes of 0.3‰ to 0.52‰.

I. Introduction

Mass transfer can be found broadly in various physical and chemical processes [1], such as gas absorption (mostly in liquids) [2], liquid evaporation [3], liquid-liquid extraction [4] and, for many cases, chemical reactions [5-7]. Revealed by two prevalent models of mass transfer, i.e., the film model [8] and the penetration model [2] developed from gas-liquid absorptions, molecular diffusion of the solute across the interface and exposure time of the liquid solvent to the solute at the interface are two key factors, apart from the solubility limit of the solute in the liquid, for the mass transfer rate. This finding indicates that the mass transfer can be controlled by regulating the molecular diffusion and the contacting time, which can be achieved from either the apparatus or the fluid side [9]. On the other hand, it elucidates why unique macroscopic apparatus (e.g., bubbling columns and film reactors) and stirring strategies for increasing interfacial area or adding disturbance on the solvent side have been developed and implemented extensively [10,11]. Nevertheless, mass transfer within those conventional apparatus may be still a bottle-neck to intrinsically rapid kinetics featured reactions [12,13] due to the flow condition (e.g., superficial velocity, flow regime, etc.) *in situ* and the surface-to-volume ratio of the reactants. In addition, particularly for bubbles/drops/films involved macroscale reactors or contactors, one limitation is that the size distribution of gas or liquid segments may be compromised or difficult to be narrowed given hydrodynamic uncertainties (e.g., eddies) [14-16], which is manifested when compared to microscale systems characterized with low Reynolds numbers (≪ 100 and often < 1) and capillary numbers (often < 1) [17-21].

Microfluidics as well as µTAS (micro total analysis systems) have rapidly progressed over the last twenty years [22-24], and have become promising alternatives to the conventional apparatus. Some merits of microfluidics may include, but are not limited to, large surface-volume ratios, enhanced mass transfer performance, predictable and uniform gas/liquid segments, convenient controls of reaction parameters and increased securities. Besides, kinetics of chemical processes and the fluid-fluid mass transfer performance could be revealed and characterized, respectively [25-28]. Analogous to studies related to conventional apparatus, gas-liquid biphasic systems as well as interphase mass transfer characteristics (e.g., mass transfer coefficient) are a research focus within the microfluidics sector too [29-34]. Liquid-liquid systems, with most interests in interphase mass transfer based extractions, emulsions and reactions have been probed as well in capillary- and microchannel-based reactors [35-40]. For both gas-liquid and liquid-liquid systems, various flow regimes (e.g., bubbles, drops, slugs, annular and parallel flows) that result from different flow geometries, fluid properties and/or flow

conditions [41-44] are very likely to influence the mass transfer that mainly occurs at the interface [42], though the influence might also be insignificant [45]. Among all flow regimes, Taylor flow (maybe also referred slug, bubble train, segmented or intermittent flow) has become a widely studied one [7,46]. Taylor segments (bubbles or drops) are generally characterized with a Bond number (Bo = $\Delta\rho g d^2/\sigma$) smaller than 3.37 and a capsular form whose equivalent diameter is times of the channel (hydrodynamic) diameter. The popularity of Taylor flow in interphase mass transfer studies, as discussed [7,46,47], is mainly due to: (1) the stability and predictability of the flow regime, (2) well-defined hydrodynamic characteristics (e.g., morphology, monodispersity, size, speed, thickness of the thin film that encloses the drop and separates the liquid slugs from one another, etc.), and (3) re-circulations within both liquid slugs and drops that could enhance heat and mass transfer [48-50].

Gas-liquid and liquid-liquid systems at Taylor flow regime within microscale devices have been massively studied [7]. Among the fluids, carbon dioxide (CO_2) has started to be attempted in the past decade (particularly since 2010) with main interests in microscale fluid dynamics and chemical processes. These attempts are usually driven by: (1) the environmental role of CO_2 as one of the major greenhouse gases in climate change, and (2) the physical and chemical properties of CO_2 based on which chemical reactions and material syntheses may be carried out in an efficient as well as a green way [51]. Accordingly, a few mitigation strategies including CO_2 capture and storage (CCS) have been proposed to reduce industrial emissions and to bar atmospheric CO_2 concentrations [52], and dense CO_2 including liquid and supercritical state has been expected for green chemistry [53,54]. Regardless of the motive and the attempt related with CO_2, mass transfer of CO_2 itself in multi-scale processes such as extraction based CO_2 captures, pipeline transports, geological storage and chemical reactions is always a key issue. Different from an immiscible fluid pair (e.g., water-oil), CO_2 together with an aqueous liquid may be a partially miscible one. Driven by a series of mechanisms, e.g., physical absorption (or dissolution), diffusion and reactions with the solvent, CO_2 Taylor bubbles or drops are likely to shrink due to the mass transfer mainly on and across the interface, the magnitude of which depends on the spatial and the temporal scale as well. Sun and Cubaud [55] experimentally studied the dissolution rate of CO_2 bubbles shortly after initial contacts with three liquids (water, ethanol, and methanol) in a flow focusing device and showed that the shrinkage (in terms of bubble length reduction) was almost linear with time. Later, Cubaud et al. [56] focused on CO_2-water at an extended microchannel length (~10^3 times of channel width) and reported not only CO_2 bubble shrinkage but also a flow regime transition (segmented to bubbly flow) at very much downstream. Also in a microfluidic flow focusing device, CO_2 bubbles experienced a shrinkage-recovery-shrinkage (termed "bubble breathing") transition subjected to varying temperatures [57]. Detailed studies of CO_2 dissolution and solubility in dimethyl carbonate (DMC) were performed in a microscale device by the same group [58]. A similar strategy for screening CO_2 solubilities in pure and mixed solvents based on bubble shrinkage in a microfluidic device was provided by Lefortier et al. [59]. Using gas CO_2 and sodium dodecyl sulfate (SDS) solution in a flow focusing microfluidic device, Shim et al. [60] reported two dissolution regimes during CO_2 bubble flow, namely, a rapid size decreasing period (~30 ms) and a subsequent equilibrium regime during which gas was exchanged between the bubble and the liquid phase. Moreover, the mass transfer coefficient of gas CO_2 was investigated at a Taylor flow regime in a microchannel and significant shrinkage effects of CO_2 segments were reported [61]. However, none of these studies are related to dense CO_2, and very few literature have reported on the shrinkage effect of dense CO_2 drops or segments, especially in a hydrodynamic scenario.

In this work, liquid CO_2 under a Taylor flow regime is going to be studied in a uniquely fabricated microfluidic device. De-ionized (DI) water is used as the solvent as well as a continuously flowing liquid. A micro T-junction is applied to produce liquid CO_2 Taylor drops. With a long straight microchannel downstream, hydrodynamics and the mass transfer of liquid CO_2 drops in water are probed. In section II, a general mathematical model of the solvent-side mass transfer coefficient (k_s) is developed based on the drop volume change in a hydrodynamic scenario. Based on a detailed geometrical description of a single drop enclosed by thin films in a rectangular microchannel, a specific form of k_s is derived by meticulous formulations of the surface area

and the volume of the drop. In the second part of Section II, an overall pressure drop due to micro-segmented flows in microchannels is considered. With the calculated overall pressure drop, the Peng-Robinson equation of state [62] and the initial CO_2 pressure in the T-junction, the drop volume change subjected to the pressure drop is analyzed. Section III introduces the experimental methodology and procedures and shows an overview of observed liquid CO_2 drops at three specified positions of the channel. In Section IV, experimental results and discussions are given. Section V is a conclusion of our work.

II. Methodology

A. Mathematical model of solvent-side mass transfer coefficient (k_s)

A1. A general form of k_s

In order to formulate the solvent-side mass transfer coefficient k_s (m/s), a one-dimensional and unsteady flow problem where (pure) solute drops separated by solvent liquid segments flow at a Taylor flow regime in a long straight microchannel is considered. An incompressible flow of the drop and the solvent liquid as well as homogeneous material properties are assumed. In addition, no significant reactions are involved during the mass transfer across the interface. Despite an apparently overall unsteady state, the flow characterized by an intermittency could be deemed steady when an accompanying reference frame is induced relative to the moving drop that makes an ensemble averaging possible [63]. As a solute drop moves at speed v_1 and is characterized by length L_1, as shown in Figure 1, it may exhibit shrinkage in terms of drop length reduction due to the dissolution-diffusion resulted mass transfer across the interface. Thus, the drop length (L) becomes a function of the position (x) along the straight microchannel. Drop speed together with a certain known channel distance (x_{n+1} - x_n, n is a positive integral) provides a time scale during which an observable size reduction arises. Figure 1 shows a schematic of the liquid solute drops characterized by different lengths at different positions along a channel. Continuous phase slugs behave as solvent for solute drops and presumably maintains a constant flowing speed (v_x) spanning the overall length of the straight channel. The cross section of the microchannel is defined rectangular and its width and depth are denoted by W (see Figure 1) and D (not shown in the schematic but deemed perpendicular into paper), respectively.
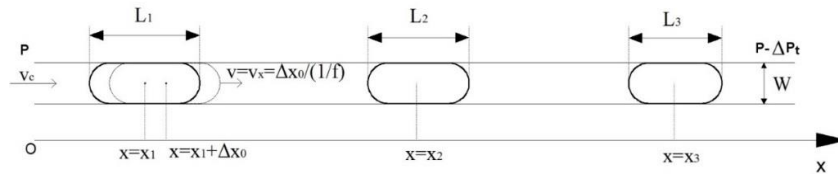

Figure 1. Schematic of shrinking drops in the other liquid at a Taylor flow regime in a straight microchannel. L_x and v_x indicate drop length and speed at position x (x = 1, 2, 3…), respectively; v_c is the superficial flowing speed of the continuous fluid over the cross-section of the microchannel; 'f' used in the calculation of v_x is a frame rate (frames per second, fps) of image acquisition in practice. An overall pressure drop (ΔP_t) is noted as well.

According to the conservation and a quasi-steady state assumption of the mass transfer, k_s (m/s) over an infinitesimal time can be defined as

$$k_s A \Delta C_s = \dot{n}_d, \tag{1}$$

where A is the effective mass transfer interfacial area, m^2; ΔC_s is a concentration difference on the solvent side adjoining the interface that drives the mass transfer, mole/m^3; and $\dot{n}_d$ is the molar flux of the mass transfer, mole/s. $\dot{n}_d$ can also be concisely defined from the viewpoint of mass transfer, i.e.,

$$\dot{n}_d = \frac{dn}{dt} = \frac{1}{M}\frac{dm}{dt} = \frac{1}{M}\frac{d(\rho V)}{dt} = \frac{1}{M}\frac{\rho d(V) + V d(\rho)}{dt}, \tag{2}$$

where ρ, V and M are the density (kg/m^3), the volume (m^3) and the molecular weight (kg/kmol) of the solute drop, respectively. Due to incompressible flow, the density of the solute drop is a constant which is irrelevant to time in a specific hydrodynamic scenario. Therefore, $d(\rho)/dt$ equals to 0, and equation (2) can be simplified as

$$\dot{n}_d = \frac{1}{M}\frac{\rho d(V)}{dt}, \tag{3}$$

Towards a mathematical model, the solute drop is assigned with a nominal molar concentration C_d (mol/m^3) and

$$C_d = \frac{\rho}{M}. \tag{4}$$

Combine equation (3) and (4), we have

$$\dot{n}_d = C_d \frac{d(V)}{dt}, \tag{5}$$

by which the mass transfer is correlated to the solute drop shrinkage in terms of drop volume change over time. Substitute equation (5) to (1) gives

$$k_s A = \frac{C_d}{\Delta C_s}\frac{d(V)}{dt}. \tag{6}$$

One of the main interests in this problem is the solute drop length reduction, or say, the volume reduction thanks to the diffusion-controlled dissolution in a hydrodynamic circumstance. A sharp interface (thickness ~ 0) separating the solute drop from the solvent slug very likely feature an equilibrium concentration in a saturation scenario, where this equilibrium concentration is denoted by C_e (mol/L). Provided that the mass transfer is a limited one and based on a known hydrodynamic circulating condition near the interface that homogenizes the bulk solvent slug, the bulk of the solvent slug is practically of a zero concentration (i.e., $C_\infty = 0$). The concentration difference ($C_e - C_\infty$) on the solvent side forms a driving force for the molar flux. Hence, the concentration difference ΔC can be expressed by

$$\Delta C_s = C_e - 0 = C_e. \tag{7}$$

Substitute equation (7) into (6), we have

$$k_s = \frac{1}{A}\frac{C_d}{C_e}\frac{d(V)}{dt}. \tag{8}$$

C_d and C_e are presumably known as long as fluids are known. A and V are overall functions of time. Equation (8) is a general form of k_s in infinitesimal time during which a constant surface area of the drop still maintains.

A2. A specific form of k_s

As shown by equation (8), the effective surface area (A) and the drop volume (V) of the solute drop need to be determined in order for the mass transfer coefficient. To obtain A and V via readily accessible parameters that are either known or measurable, a single Taylor drop is considered in a rectangular microchannel under a three-dimensional (3D) scenario. Figure 2 shows a solute drop flowing a microchannel that has a width W and a depth D (D ≤ W). As shown in Figure 2b, 2c and 2d, a thin film (with thickness δ at the channel wall and thickness δ' at the channel corner) of the continuous fluid enclosing the drop exists between the drop and the channel wall and prevents the drop from contacting the wall. This film results from a wall wettability preferrence to the continuous fluid over the solute fluid. The drop is characterized with an end-to-end length L and two principal radii of curvature (i.e., R_w and R_d) of its meniscus, see Figure 2b and 2c. R_w and R_d can be derived by inducing the contact

4

angle θ_c between the drop and the continuous fluid at wall, see Figure 3. Here, R_w is chosen as an example showing how the radii of curvature of the drop meniscus is determined. Focusing on the triangle denoted by a right angle symbol in Figure 3, two geometric equations can be written,

$$R_w \cdot \cos(\pi - \theta_c) = W/2 - \delta, \tag{9}$$

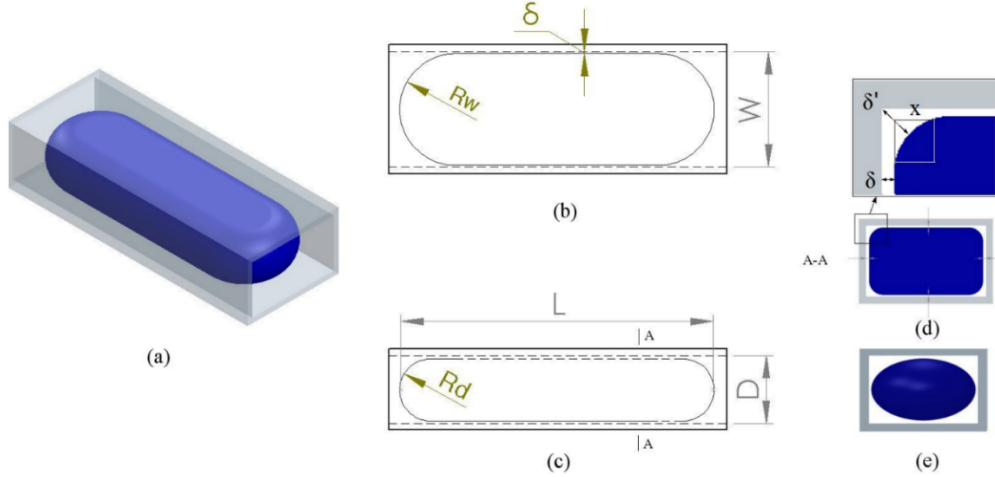$$R_w \cdot \sin(\pi - \theta_c) + L_{c,w} = R_w. \tag{10}$$

Figure 2. Schematics of one single Taylor drop in a rectangular microchannel (width: W, depth: D). (a) A 3D view of the drop in the microchannel; (b) a top view of the drop showing the channel width W, the thickness (δ) of the thin film of the continuous fluid, and the radii of curvature R_w in a projected plane; (c) a side view of the drop showing the drop length L, the channel depth D, and the radii of curvature R_d in a projected plane; (d) A-A sectional view of the drop where the thin film is of thickness δ at the channel wall and thickness δ' at channel corners (see the inset); (e) a projected right view of the drop meniscus.
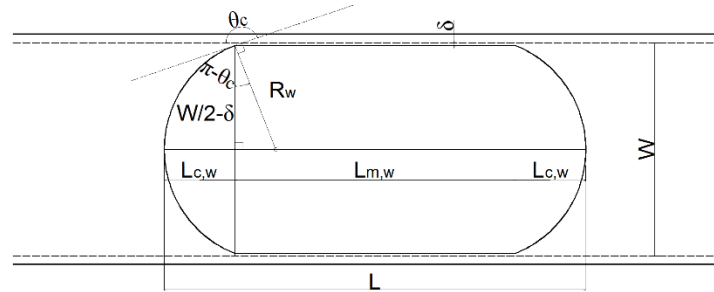

Figure 3. Geometrical descriptions of one single Taylor drop in a microchannel. The ellipse symbolizes the drop. Two horizontal dash lines at the top and the bottom indicate the inner channel wall. The drop is presumably composed of two meniscuses and a main part in the middle. A transitional surface section may exist at between the drop meniscus and the middle part.

After rearranging, R_w and $L_{c,w}$ can be obtained as

$$R_w = \frac{W/2 - \delta}{-\cos\theta_c}, \tag{11}$$

and

5

$$L_{c,w} = \frac{W/2 - \delta}{-\cos\theta_c}(1 - \sin\theta_c), \tag{12}$$

respectively. Further, the length of the drop main part, i.e., $L_{m,w}$ (see Figure 3), can be determined from deducing $2L_{c,w}$ from the total length L, i.e.,

$$L_{m,w} = L - 2L_{c,w} = L - \frac{W - 2\delta}{-\cos\theta_c}(1 - \sin\theta_c). \tag{13}$$

Next, the surface area and the volume of the drop will be solved based on a three-portion composition assumption of the drop, i.e., two drop meniscuses and one main middle part (see Figure 3). Accordingly, the surface area and the volume of the drop are formulated as

$$A = 2A_{c,w} + A_{m,w}, \tag{14}$$

and

$$V = 2V_{c,w} + V_{m,w}, \tag{15}$$

where $A_{c,w}$ and $V_{c,w}$ are the surface area and the volume of the drop cap, $A_{m,w}$ and $V_{m,w}$ are those of the middlel part of the drop. The drop cap is approximated one half of a general triaxial ellipsoid whose semi-axes are (W/2 - δ), (D/2 - δ) and $L_{c,w}$, respectively, see Figure 2e and Figure 3. To determine $A_{c,w}$, an approximation (Thomsen's formula) proposed by Knud Thomsen [64] is applied, i.e.,

$$A_{c,w} \approx 2\pi\left\{\left[\left(\frac{W}{2} - \delta\right)^p\left(\frac{D}{2} - \delta\right)^p + \left(\frac{W}{2} - \delta\right)^p L_{c,w}{}^p + \left(\frac{D}{2} - \delta\right)^p L_{c,w}{}^p\right]/3\right\}^{\frac{1}{p}}, \tag{16}$$

the least relative error when p ≈ 1.6075 is within ±1.061%. Moreover, the volume $V_{c,w}$ is calculated as follows,

$$V_{c,w} = \frac{4}{3}\pi\left(\frac{W}{2} - \delta\right)\left(\frac{D}{2} - \delta\right)L_{c,w}. \tag{17}$$

Prior to calculating $A_{m,w}$ and $V_{m,w}$, the perimeter and the area of the cross section of the drop middle part that is perpendicular to the flowing direction (see Figure 2d) need to be determined. By referring to the film thickness at the channel wall and wall corners, as shown in the local enlarged view in Figure 2d, the perimeter and the area of the drop cross section are 2(πx + W + D - 4δ - 4x) and [WD - 2δ(W + D) - (4 - π)x^2 + 4δ^2], respectively, in which $x \approx \frac{\delta' - \sqrt{2}\delta}{\sqrt{2} - 1}$. Based on literature results of Taylor bubble (or drop) flows in rectangular capillaries with Ca < 10^{-2} [58,65,66], the thin fim thickness δ and δ' at the channel wall and the channel corner may be approximated by 0.02W and 0.1W, respectively. Thus x can be simplified as 0.17W, and the perimeter and the area of the drop cross section are further simplified, respectively, as 2(0.774W + D) and (0.96WD - 0.0632W^2). Therefore, the surface area $A_{m,w}$ and the volume $V_{m,w}$ of the main middle part of the drop can be written as

$$A_{m,w} = 2(0.774W + D) \cdot L_{m,w}, \tag{18}$$

and

$$V_{m,w} = (0.96WD - 0.0632W^2) \cdot L_{m,w}. \tag{19}$$

Substitute Equation (13) into the above two equations and rearranging δ by 0.02W,

$$A_{m,w} = 2(0.774W + D) \cdot (L + 0.96\frac{1 - \sin\theta_c}{\cos\theta_c}W), \tag{20}$$

and

$$V_{m,w} = (0.96WD - 0.0632W^2) \cdot (L + 0.96\frac{1-sin\theta_c}{cos\theta_c}W). \tag{21}$$

Similarly, Equation (16) and (17) are specified as follows

$$A_{c,w} \approx 2\pi \left\{ \frac{(0.24WD-0.0096W^2)^{1.6075}}{3} + \frac{[(0.48W)^{1.6075}+(0.5D-0.02W)^{1.6075}]\cdot\left(0.48\frac{1-sin\theta_c}{-cos\theta_c}W\right)^{1.6075}}{3} \right\}^{0.6221}, \tag{22}$$

and

$$V_{c,w} = 0.32\pi W(0.5D - 0.02W) \cdot 0.96\frac{1-sin\theta_c}{-cos\theta_c}W. \tag{23}$$

Integrate equation (20) - (23) with (14) and (15), the surface area A and the volume V of a drop are formulated as

$$A = 4\pi \left\{ \frac{(0.24WD-0.0096W^2)^{1.6075}}{3} + \frac{[(0.48W)^{1.6075}+(0.5D-0.02W)^{1.6075}]\cdot\left(0.48\frac{1-sin\theta_c}{-cos\theta_c}W\right)^{1.6075}}{3} \right\}^{0.6221} + (1.548W + 2D) \cdot$$

$$(L + 0.96\frac{1-sin\theta_c}{cos\theta_c}W), \tag{24}$$

and

$$V = (0.96WD - 0.0632W^2) \cdot L + (0.0435WD + 0.0221W^2) \cdot \frac{1-sin\theta_c}{-cos\theta_c}W. \tag{25}$$

It is necessary to note that a transitional surface section (see Figure 3) from the drop meniscus to the main middle part has not been considered, instead, is incorporated to the middle part of the drop. Thus, the surface area and the volume determined by Equation (24) and (25) are likely to overestimate. The incorporation may only be appropriate when drop length L is relatively larger than the channel width W, thus the transitional area compared with the realistic middle part becomes small. Additionally, the above formulation are generally based on that the volume of the drop middle part is larger than that of the two caps, i.e., $V_{m,w} > 2V_{c,w}$, thus there exists a critical drop length L (determined by W, D and θ_c) below which Equation (24) and (25) may not be applicable. It can be seen that the surface area and the volume of the flowing drop in a defined channel geometry with involved fluids being known are determinable as long as the drop length L can be measured. The solvent-side mass transfer coefficient, starting from Equation (8), can be further specified as follows

$$k_s = \frac{1}{A}\frac{C_d}{C_e}\frac{d(V)}{dt} = \frac{1}{A}\frac{C_d}{C_e}(0.96WD - 0.0632W^2)\frac{d(L)}{dt}$$

$$\downarrow$$

$$k_s\frac{C_e}{C_d}\frac{1}{(0.96WD - 0.0632W^2)}dt = \frac{1}{A}d(L)$$

$$\downarrow$$

$$\int k_s\frac{C_e}{C_d}\frac{1}{(0.96WD - 0.0632W^2)}dt = \int\frac{1}{A}d(L) = \frac{1}{(1.548W + 2D)}\int\frac{1}{A}d(A)$$

$$\downarrow$$

$$k_s\frac{C_e}{C_d}\frac{1}{(0.96WD - 0.0632W^2)}t = \frac{1}{(1.548W + 2D)}(\ln A)_{A_x}^{A_0} + B$$

7

in which B is a constant resulting from the integral. An initial condition ($A_x = A_0$, at t = 0) can be applied to determine that B = 0. Thus,

$$k_s \text{ (mm/s)} = \frac{(0.96WD - 0.0632W^2)}{(1.548W + 2D)} \frac{C_d}{C_e} \cdot \frac{1}{t}$$

$$\cdot \ln \frac{4\pi \left\{ \frac{(0.24WD - 0.0096W^2)^{1.6075}}{3} + \frac{[(0.48W)^{1.6075} + (0.5D - 0.02W)^{1.6075}] \cdot \left(0.48 \frac{1 - sin\theta_c}{-cos\theta_c}W\right)^{1.6075}}{3} \right\}^{0.6221} + (1.548W + 2D) \cdot \left(L_0 + 0.96 \frac{1 - sin\theta_c}{cos\theta_c}W\right)}{4\pi \left\{ \frac{(0.24WD - 0.0096W^2)^{1.6075}}{3} + \frac{[(0.48W)^{1.6075} + (0.5D - 0.02W)^{1.6075}] \cdot \left(0.48 \frac{1 - sin\theta_c}{-cos\theta_c}W\right)^{1.6075}}{3} \right\}^{0.6221} + (1.548W + 2D) \cdot \left(L_x + 0.96 \frac{1 - sin\theta_c}{cos\theta_c}W\right)}, \quad (26)$$

B. Pressure drop and its impact upon drop size

B1. Pressure drop over the micro channel length

A short review of some commonly referred pressure drop models of segmented flows in microchannels is provided in the Supplemental Materials (See S3 in SM). By comparisons in terms of applicability, a modified version of Warnier's model proposed by Eain et al. [67] is going to be used for calculating the total pressure drop of the Taylor flow over the microchannel length in this work. This modified Warnier's model is specified as follows

$$\Delta P_t = L_t \frac{32\eta_c \overline{v_c}}{(2R_h)^2} \left[1 + \frac{8.16 \times 3^{\frac{2}{3}}}{32} \frac{1}{L_c^*} \frac{A_c}{A_d} \frac{1}{(Ca_d^{\frac{1}{3}} + 3.34Ca_d)}\right], \quad (27)$$

where L_t and ΔP_t are the total microchannel length and the total pressure drop over the channel length, respectively. η_c and $\overline{v_c}$ are the dynamic viscosity and the superficial mean velocity of the continuously flowing slugs, the latter of which can be determined from dividing the total flow rate by the channel cross area. R_h is the hydrodynamic radius of the microchannel and $R_h = DW/(D + W)$ for a rectangular one. L_c^* is a non-dimensional length of the continuously flowing slug, and $L_c^* = L_{s,w}/(2R_h)$ in which $L_{s,w}$ indicates the slug length. In addition, (L + $L_{s,w}$) accounts for the length of a flow unit composed by a drop and a continuous slug. A_c and A_d are the channel and the bubble cross sectional area, respectively. Ca_d is the capillary number calculated on the drops.

Based on the modification of a curvature parameter from 7.16 to 8.16, the applicability of Warnier's model [68] is further extended in terms of such non-dimensional parameters: $1.45 \leq Re \leq 567.59$, $4.5 \times 10^{-5} \leq Ca \leq 0.067$, $0.76 \leq L_c^* \leq 46.83$, $1.05 \leq L_d^* \leq 14.25$, and liquid-liquid Taylor flows in micro capillaries as well. However, as noted by Warnier et al. [68], the model is partly based on the work of Bretherton [69] and Aussillous and Quéré [70] in determining the pressure drop of a single Taylor bubble. Thus, the model as well as the modified one is unlikely to be applicable to circumstances such as non-axisymmetric channels, non-laminar flows of continuous phase, strong inertia, nor non-ignorable velocity of the thin film that separates the bubble from touching the channel wall.

B2. Drop volume change subjected to pressure drop

Since a very general dispersed fluid is considered that might be either a bubble or a droplet surrounded by a continuous liquid in the Taylor flow, it is better to use a more applicable equation of state (EOS) to describe the dispersed fluid rather than a classical ideal gas law. Cubic equations, among other equations, of state in terms of volume have been proposed and developed in the past 140 years to correlate pressure, volume and temperature together for a given quantity of substances within a system, to name a few, the Van der Waals EOS [71], the Redlich-Kwong EOS [72], the Soave-Redlich-Kwong EOS [73], the Peng-Robinson EOS [62], volume-translated

EOS [74,75] and Patel-Teja EOS [76]. Despite such many cubic EOS, a generic cubic EOS [77] may be written as below

$$P = \frac{RT}{V-b} - \frac{c}{V(V+d)+e(V-d)},$$

(28)

in which b, c, d, and e are constants or functions of temperature as well as fluid properties (e.g., acentric factors, critical compressibility factors, etc.); P, V and T are pressure, volume and temperature, respectively; R is the universal gas constant. The first and the second term on the right-hand side of the above equation indicate a repulsion pressure and an attraction pressure, respectively. Among numerous cubic EOS not limited to the above ones, the Soave modified Redlich-Kwong EOS (also called Soave-Redlich-Kwong EOS) and the Peng-Robinson EOS have been the most frequently applied ones in studies related to thermo-physical and vapor-liquid equilibrium (VLE) properties. Moreover, as compared by Peng and Robinson [62] between their calculated vapor pressures of pure substances and equilibrium ratios of mixtures and those calculated by the Soave-Redlich-Kwong EOS, Peng-Robinson EOS provided slightly more accurate agreements with experimental data. Therefore, the Peng-Robinson EOS is chosen to correlate the drop volume change (viz., drop length change) with the pressure drop over the micro channel. The Peng-Robinson EOS is given below

$$P = \frac{RT}{V_m - b(T_c)} - \frac{c(T_c)\beta(T_r,\omega)}{V_m[V_m+b(T_c)]+b(T_c)[V_m-b(T_c)]},$$

(29)

in which

$$b(T_c) = 0.07780\frac{RT_c}{P_c}, \qquad c(T_c) = 0.45724\frac{R^2T_c{}^2}{P_c},$$

$$\beta(T_r,\omega) = [1 + (0.37464 + 1.54226\omega - 0.26992\omega^2)(1 - T_r{}^{0.5})]^2,$$

(30)

where P_c, T_c and V_m are the critical pressure, the critical temperature and the molar volume (V_m: volume/mole), respectively; $\beta(T_r, \omega)$ is a non-dimensional function of temperature ratio T_r ($T_r = T/T_c$) and an acentric factor ω of the specific substance (ω for common hydrocarbons and N_2, CO_2, H_2S are referred to the figure 2 in Peng and Robinson's original paper [62].). If temperature (T) is a constant, equation (29) for a known fluid becomes an equation with two unknown variables, i.e., P and V_m. Furthermore, two such equations may be available at the starting and the ending point of the straight channel, and an equation set including these two equations can be obtained as follows

$$\begin{cases} P_0 = \frac{RT}{V_{m0}-b(T_c)} - \frac{c(T_c)\beta(T_r,\omega)}{V_{m0}[V_{m0}+b(T_c)]+b(T_c)[V_{m0}-b(T_c)]}, \\ P_t = \frac{RT}{V_{mt}-b(T_c)} - \frac{c(T_c)\beta(T_r,\omega)}{V_{mt}[V_{mt}+b(T_c)]+b(T_c)[V_{mt}-b(T_c)]}, \text{ and} \\ \Delta P_t = (P_0 - \frac{\sigma\cos\theta_c}{R_h}) - (P_t - \frac{\sigma\cos\theta_c}{R_h}) = P_0 - P_t. \end{cases}$$

(31)

If P_0 is known in practice, together with the pressure drop determined by equation (27), P_t at the ending point of the microchannel can be determined and then used to solve out the two unknowns, i.e., V_{m0} and V_{mt}, where subscript '0' and 't' indicate the parameter at the starting and the ending point, respectively. Based on solved V_{m0} and V_{mt}, the relative volume change of the drop $\Delta V/V_0$ due to the pressure decrease can be calculated by

$$\Delta V/V_0 = N \cdot \Delta V_m/V_0 = N \cdot (V_{mt} - V_{m0})/(N \cdot V_{m0}) = \frac{V_{mt}}{V_{m0}} - 1.$$

(32)

According to equation (27), (31) and (32), an estimated (or directly measured) initial pressure and a (quantitative) knowing of the Taylor flow in the microchannel are required in order to obtain the drop volume change subjected to the pressure decrease. However, such a clear idea of the drop volume change will not be possible without any

experiments or numerical methods. Next, a series of experiments is going to be carried out in which liquid CO_2 and water are used as a drop fluid and a continuous liquid, respectively, in Taylor flow regimes.

III. Experiments

A. Setup

The experimental system (see Figure S1 in SM) introduced in our previous work [78] is applied here to undertake the hydrodynamic dissolution of pressurized Taylor drops in a straight microchannel. In brief, two mechanical syringe pumps (Teledyne Isco 260D and 100DM) are used to deliver two different fluids to the microfluidic system comprised of a self-made non-permanent connector and a silicon-glass microchip. The connector bridges the large-scale stainless steel tubing to the microchip. The fabrication of the microchip is mainly fulfilled by, in sequence, standard photolithography, deep reactive ion etching (DRIE), inlet & outlet drilling, anodic bonding of silicon and glass wafer, and dicing (of bonded wafers) into a final rectangular shape ($74 \times 44 \times 1.2$ mm^3). As shown by Figure 4, a micro T-junction in the microchip is applied to produce Taylor drops in the microchannel. In particular, liquid carbon dioxide (purity 99.9%, Praxair Canada) is used as a dispersed fluid which is injected at constant flow rates into the side channel of the T-junction; de-ionized (DI) water is used as the continuous liquid flowing at various constant flow rates in the main channel. One specific flow case is characterized by a constant flow rate ratio, i.e., Q_{LCO2}/Q_{H2O}. The side channel, main channel as well as the downstream straight microchannel (total length = 14.7 mm) are all characterized by a uniform width (W) of 150 μm and a uniform depth (D) of 100 μm. Although not shown, the further downstream to the end of the straight channel features a 90° turning first and a 55 mm long microchannel which eventually connects to the outlet of the connector. The back pressure of the flowing system is controlled by a back pressure regulator (model EB1ULF1, Equilibar) together with a needle valve. A nitrogen gas tank provides a reference back pressure at the back pressure regulator. However, practical back pressures during experiments are measured by a pressure transducer (Swagelok) installed between the connector and the back pressure regulator. A circulating water bath (Thermo Scientific) for maintaining a constant temperature (i.e., 25°C) of CO_2 from within the pump cylinder, through the stainless steel tubing, up to the microchip is used.
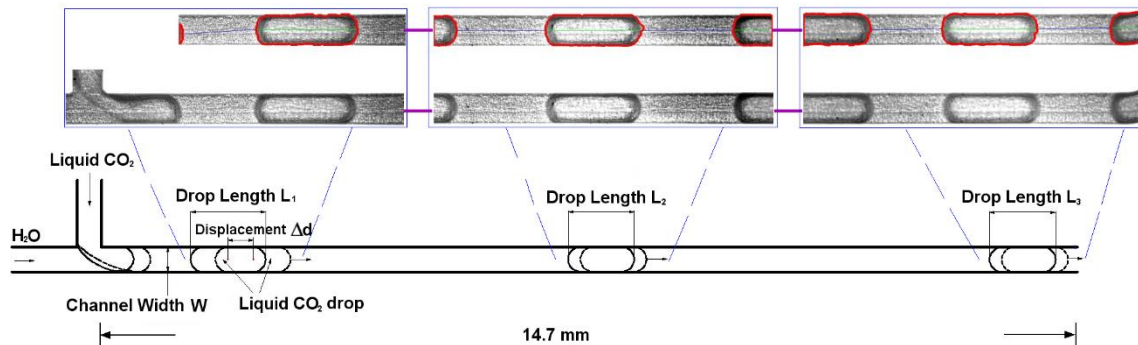

Figure 4. Schematic of the experimental methodology for investigating liquid CO_2 drops' shrinkage in a straight microchannel ($16 < L_t/L_x < 60$, x = 1, 2, 3; W = 150 μm). Drop length L_x is monitored and measured at three positions, i.e., immediately after the drop generation (position 1), at the midpoint of the microchannel length (position 2) and at the end of the microchannel (position 3). Total microchannel length L_t is 14.7 mm.

B. Measurements

The experimental methodology for studying the dissolution caused Taylor drop shrinkage is schematically introduced in Figure 4. The liquid CO_2 drop at three sequential positions of the straight microchannel, i.e., immediately after the drop generation (position 1), the midpoint of the microchannel (position 2) and the end of

the microchannel (position 3), are visualized by using an upright microscope (BX51, Olympus) combined with a high speed camera (v210, Phantom). Images-stacked videos (3000 fps (frames per second)) are recorded separately at the three positions after a waiting time of 20 minutes, each time when a different Q_{LCO2}/Q_{H2O} is applied, in order for a stable flow state. Later, these videos are first cropped into a constant size of 800×200 pixels (1 pixel ≈ 2 μm), and then analyzed in Matlab (R2014a, The Mathworks, Inc.) by using a series of self-developed Matlab codes based on identifying drops. Drop length (measured from the vertex of the back meniscus to that of the front one of the drop in the flow direction) and drop speed are the two main parameters extracted from the video analysis. Under a given Q_{LCO2}/Q_{H2O} at one of the positions, the drop length is measured for all emerging drops in the video, and the averaged value is considered a characteristic drop length, i.e.,

$$L_x = \frac{1}{N}\sum_{i=1}^{N} L_{i,x}, \qquad x = 1, 2 \text{ or } 3, \tag{33}$$

and the standard deviation s_{Lx} is calculated by

$$s_{L_x} = \sqrt{\frac{1}{N-1}\sum_{i=1}^{N}(L_{i,x} - L_x)^2}, \qquad x = 1, 2 \text{ or } 3, \tag{34}$$

where N is the total number of complete drops that have emerged in the video at position x (x = 1, 2 or 3). If one single drop of the N drops has been presented as a complete one (i.e., both its front and back meniscus are simultaneously visible in the video) from the jth frame to the $(j + M)^{th}$ frame, an average speed (v_{sd}) of this drop at this position is determined by

$$v_{sd} = \frac{1}{M}\sum_{h=1}^{M} v_{h\to(h+1)}, \tag{35}$$

where $v_{h\to(h+1)}$ is the speed of this single drop calculated from two consecutive frames, i.e., the hth and the $(h+1)^{th}$ frame ($j \leq h < M$), as formulated below

$$v_{h\to(h+1)} = \frac{\Delta d_{h\to(h+1)}}{1/fps}, \tag{36}$$

in which Δd is the drop displacement from the hth and the $(h+1)^{th}$ frame. Based on v_{sd}, of one single drop, drop speed v_x by averaging on all the drops is considered a characteristic speed, which is calculated as follows,

$$v_x = \frac{1}{N}\sum_{i=1}^{N}(v_{sd})_{i,x}, , \qquad x = 1, 2 \text{ or } 3, \tag{37}$$

and the standard deviation s_{vx} is determined by

$$s_{v_x} = \sqrt{\frac{1}{N-1}\sum_{i=1}^{N}[(v_{sd})_{i,x} - v_x]^2}, \qquad x = 1, 2 \text{ or } 3, \tag{38}$$

C. Observations

Figure 5 provides an overview of all liquid CO_2 drops under Taylor flow regime at the specified three positions of the straight microchannel for a total of nine flow rate conditions. Here, the flow rate ratio Q_{LCO2}/Q_{H2O} is tuned from 20/80 to 75/25, and ($Q_{LCO2} + Q_{H2O}$) has been controlled as a constant 100 μL/min. The capillary number (Ca_c) calculated by the water flow ($Ca_c = \eta_c v_c/\gamma$) ranges from 8×10^{-4} to 2.5×10^{-3}. The viscosity ($\eta_c = 890$ μPa·s) [79] and the interfacial tension ($\gamma = 31.7$ mN·m^{-1}) [80,81] are referred to 298 K and 65 bar, respectively. Using the same reference, the viscosity of liquid CO_2 in our work is around 58 μPa·s, thus a viscosity ratio (η_d/η_c) of 0.065 is used here. In addition, the Schmidt number ($Sc_c = \eta_c/(\rho_c D_{dc})$, where ρ_c and D_{dc} are the water density and the CO_2 diffusivity in water, respectively.) of water is calculated around 593, for which D_{dc} is approximately 1.5×10^{-9} m^2/s [82]. The superficial velocity of water, i.e., v_c, results from dividing Q_{H2O} by the cross sectional area (WD) of the channel.

At position 1, liquid CO_2 drop generations are periodic, and the length of the generated drops increases as Q_{LCO2}/Q_{H2O} increases from 20/80 to 75/25. At position 2 and 3, CO_2 drops also periodically emerge in the imaging frames, and they flow in from the left side and out on the right side. The drop length and the drop speed, at each of the three positions, are measurable based on the aforementioned methodologies. It is noted that when $Q_{LCO2}/Q_{H2O} > 75/25$ a complete drop can not be captured by our imaging methods at position 1, and when $Q_{LCO2}/Q_{H2O} < 20/80$ the generation of Taylor drops becomes unstable and non-periodic. Therefore, flow rate conditions characterized by Q_{LCO2}/Q_{H2O} beyond these two thresholds are not probed in our work.
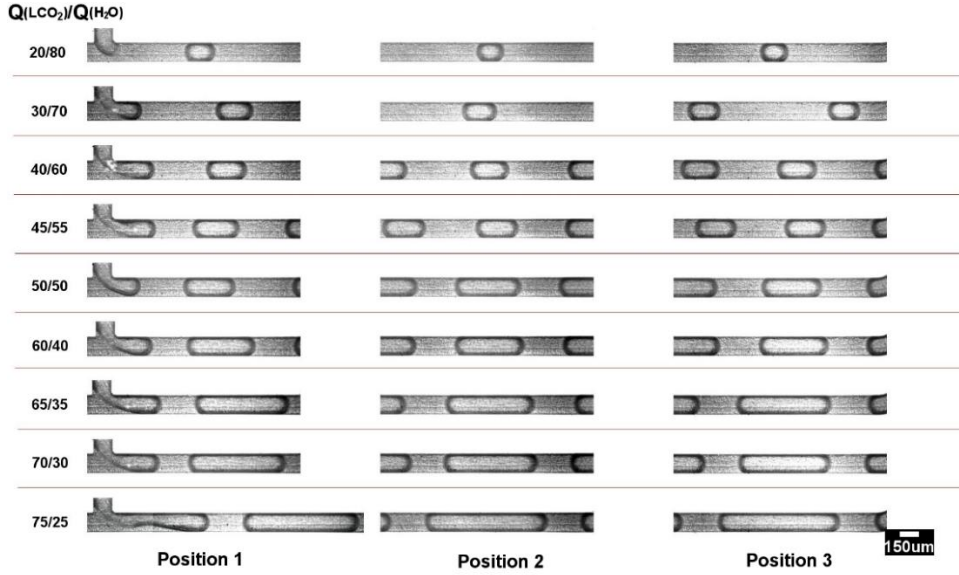
Figure 5. Snapshots of liquid CO_2 drops at three specified positions in the straight microchannel under various Q_{LCO2}/Q_{H2O}. The scale bar for all images is 150 μm. The image video at position 1 for $Q_{LCO2}/Q_{H2O} = 75/25$ results from combining two images in an end-to-end way for showing both the T-junction and a completely generated drop.

IV. Results and discussions

A. Size of the generated liquid CO_2 drop

The length (L_1) of the generated liquid CO_2 drop at the micro T-junction has been measured and normalized by the microchannel width (W). Normalized drop lengths (i.e., L_1/W) are plotted against the Q_{LCO2}/Q_{H2O} of the investigated cases, as shown in Figure 6a.
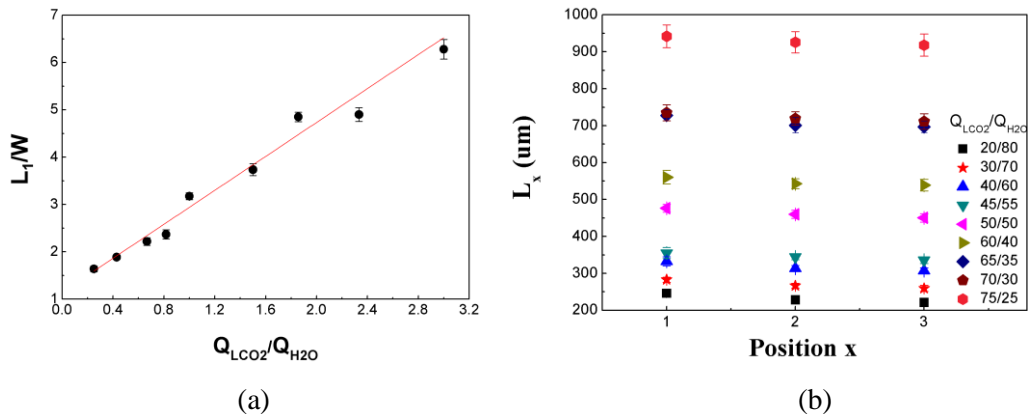

(a)

(b)

12

Figure 6. (a) Non-dimensional lengths (L_1/W) of generated liquid CO_2 drops at the micro T-junction under various Q_{LCO2}/Q_{H2O}; (b) Lengths of the liquid CO_2 drops at the three positions (x = 1, 2 and 3) under various Q_{LCO2}/Q_{H2O}. Each error bar indicates one standard deviation of the mean drop length (i.e., the data point).

The drop length increases from around 1.5W to 6.3W when Q_{LCO2}/Q_{H2O} ascends from 0.25 to 3. These data points are fitted with a method analogous to that having been applied in our previous work [78], i.e., a linear relation between L_1/W and Q_{LCO2}/Q_{H2O} (i.e., the ratio defined by the flow rate of the dispersed fluid to that of the continuous fluid). The fitting line, $L_1/W = 1.15 + 1.79 \cdot (Q_{LCO2}/Q_{H2O})$, is shown in Figure 6, which is characterized by an adjusted R-squared of 0.97. The Y-intercept is approximately 1 with a 15% deviation and the slope is 1.79 that is much larger than 1. The factor underlying the slope is related to the squeezing-elongating stage within a period of the drop generation, which has been elucidated previously [78]. The fitting, on the other hand, suggests that distinctly sized Taylor drops in terms of non-dimensional drop length can be produced by simply tuning the applied flow rate ratio in a constant micro T-junction device. However, there should exist an upper limit of Q_{LCO2}/Q_{H2O} beyond which Taylor flow starts to vanish and co-flow regimes occur, as evidenced in our previous work [78]. Drop lengths at the midpoint (position 2) and the ending point (position 3) of the long straight microchannel are measured as well. Figure 6b shows the absolute length of the liquid CO_2 drop at the three specified positions under various Q_{LCO2}/Q_{H2O}. As shown, for each flow rate condition, there is always a slight decline tendency of the drop length from position 1 to 2 and to 3, and the declines are approximately linear. The drop length tendency qualitatively describe the drop shrinkage which is considered a result of the dissolution-diffusion mechanism across the interface between the CO_2 drop and the continuously flowing water.

B. Length reduction of liquid CO_2 drops

Detailed drop length reductions are plotted against Q_{LCO2}/Q_{H2O} in Figure 7a. Here, three length reductions, namely, a total length reduction ΔL ($\Delta L = L_1 - L_3$), a first length reduction ΔL_1 ($\Delta L_1 = L_1 - L_2$), and a second length reduction ΔL_2 ($\Delta L_2 = L_2 - L_3$) are calculated and shown. The scattering data points of respective length reductions are linearly fitted by keeping the slopes as zeros. The mean values of drop length reductions ΔL, ΔL_1 and ΔL_2 are 24.35 µm, 16.52 µm and 7.83 µm, respectively. Correspondingly, the standard errors of these mean drop length reductions are 1.08 µm, 1.71 µm and 1.17 µm, respectively, which are calculated from dividing the standard deviations (see equation 34) by the square root of the sample size (i.e., 9 in our work). These mean drop length reductions may be able to be comprehended in such a way that, regardless of the sizes of the CO_2 drops being produced from the T-junction and investigated later in the microchannel, absolute values of ΔL, ΔL_1 and ΔL_2 resulted from the interphase mass transfer from CO_2 to water are generally constants, despite of two deviants that occur at $Q_{LCO2}/Q_{H2O} = 45/55$ and $Q_{LCO2}/Q_{H2O} = 65/35$.

To evaluate the total length reductions relative to the original drop length, $\Delta L/L_1$ for all cases are plotted as a function of the flow rate ratios, as shown in Figure 7b. It is obvious that, although the total drop length reductions (ΔL) may be a constant for all cases, $\Delta L/L_1$ is likely to be an exponential decreasing function (whose base is between 0 and 1) of increasing Q_{LCO2}/Q_{H2O}. This result is rational in view of the larger surface-to-volume ratios of smaller drops that are produced by lower Q_{LCO2}/Q_{H2O} which further enhance the mass transfer through the interface between CO_2 drops and the continuous flowing water. Also plotted in Figure 7b are averaged coefficients of variations (COVs) of the drop lengths at those three positions. Here, the COV of drop lengths at each position is defined by dividing the standard deviation over the mean drop length as follows

$$COV_x = \frac{s_{L_x}}{L_x}, \qquad x = 1, 2 \text{ or } 3, \tag{39}$$

where L_x and s_{L_x} are calculated from equation (33) and (34), respectively. The averaged COV as a characteristic of each investigated Q_{LCO2}/Q_{H2O} is obtained from averaging the ones at position 1, 2 and 3, as determined by

$$COV_{Q_{LCO2}/Q_{H2O}} = \frac{1}{3}\sum_{x=1}^{3}\frac{s_{L_x}}{L_x}, \qquad x = 1, 2 \text{ or } 3. \tag{40}$$

The averaged COVs behave as a measure of the variability extent of the mean drop length for each flow rate condition. For almost all the flow rate conditions, averaged COVs are approximately a constant with a value of 0.029 ($\pm$ 0.003), and vast majority of them are well below the relative drop length reductions except for Q_{LCO2}/Q_{H2O} = 75/25. This comparison, in general, shows that the drop length reductions are beyond the error scopes and can be the real characteristics of drop shrinkage.
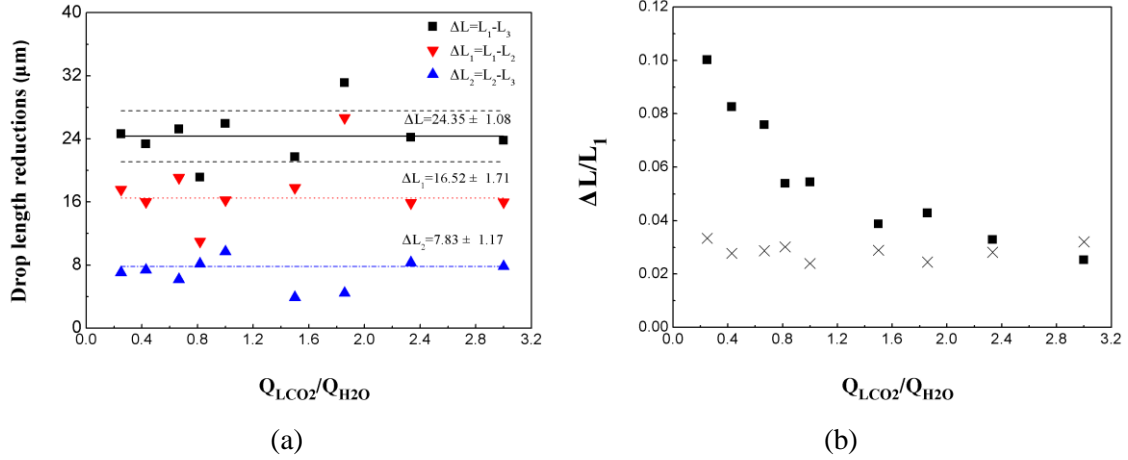

(a)   (b)

Figure 7. (a) Shrinkage of liquid CO_2 drops quantified by drop length reductions (ΔL, ΔL_1 and ΔL_2) and linear fitting lines (horizontal) of the three calculated drop length reductions, ΔL ($\blacksquare$): a total length reduction, $\Delta L = L_1 - L_3$; ΔL_1 ($\blacktriangledown$): a first length reduction, $\Delta L_1 = L_1 - L_2$; and ΔL_2 ($\blacktriangle$): a second length reduction, $\Delta L_2 = L_2 - L_3$. Solid line is a fitting line of ΔL, and a positive and a negative one standard deviation band (dash lines above and below the solid line) of the mean ΔL are added for reference. (b) Relative total drop length reductions $\Delta L/L_1$ ($\blacksquare$) versus averaged coefficients of variations (COVs) of drop lengths ($\times$) at various flow rate ratios.

C. Pressure drop and resulted drop volume change

C1. Total pressure drop ΔP_t

With experimentally obtained drop and slug lengths and by revisiting the section II. B, the pressure drop and the drop volume change can be evaluated according to equation (27) and (32). Nevertheless, the length of the continuous slugs needs to be known and an estimate of the initial pressure (P_0) at the micro T-junction is required as well in order to determine the pressure drop ΔP_t. Figure 5, on the other hand, delivers an intuitive scene of the slug between two consecutive drops. However, the case Q_{LCO2}/Q_{H2O} = 20/80 is unable to show a complete slug length due to a size limitation of our field of view (1650 μm $\times$ 380 μm) in which CO_2 drops are prioritized. Detailed water slug lengths, under all other flow conditions, have been measured at each of the three positions and are plotted similarly as for drop lengths, as shown in Figure 8. Almost all the cases except Q_{LCO2}/Q_{H2O} = 30/70 are characterized by invariant slug length (relative total slug length increases ($L_{s3,w}$-$L_{s1,w}$)/$L_{s1,w}$ $\le$ 0.08), which may be also true for Q_{LCO2}/Q_{H2O} = 30/70 considering the error having been introduced by the syringe pump operating at lower flow rates.

Shown by equation (27), ΔP_t is inversely proportional to the non-dimensional slug length L_c^*. Next we are going to calculate the pressure drops in a further-case scenario by using the nominal minimum slug length among the ones at position 1, 2 and 3, which may introduce somewhat overestimated pressure drops. Apart from L_c^*, other parameters on the right-hand side of equation (27) are listed in Table 1 and their physical meanings and determinations are briefly introduced in the table annotations. Based on Table 1 and equation (27), the pressure

14

drop over the practical total length of the straight microchannel is calculated and has been plotted against Q_{LCO2}/Q_{H2O} in Figure 9a. Although there exists a slight decrease of ΔP_t subjected to increasing Q_{LCO2}/Q_{H2O} from 30/70 to 75/25, the decrease compared to the pressure drop is very insignificant. Variations of ΔP_t are within 1.6% of a mean value of $\Delta P_t = 3175.383$ Pa. Despite a constant ΔP_t, the decreasing trend of ΔP_t subjected to an increasing Q_{LCO2}/Q_{H2O} (i.e., a larger CO_2 drop length fraction and a smaller water slug length fraction in the entire channel) reflects a dominant role of the water slugs in controlling the pressure drop. Moreover, it is also noticed that the contribution of the second term on the right-hand side of equation (27) (non-dimensional as well) to the pressure drop, comparatively, is almost two orders of magnitude smaller than the water as a continuous fluid.

Table 1. The parameters that are applied to calculate the pressure drops over the total channel length by equation 27.

Q_{LCO2}/Q_{H2O}	$\eta_c \times 10^6$ (Pa·s)	$\bar{v}_c[1] \times 10^3$ (m/s)	$Ca_d[2] \times 10^3$	$R_h[3] \times 10^6$ (m)	L_c* (1)	$A_d[4] \times 10^{12}$ (m²)	$A_c[5] \times 10^{12}$ (m²)	$L_t[6]$ (mm)	$L_t'[7]$ (mm)	$P_0[8]$ (10^5 Pa)
30/70	930.32	111.11	2.88	60	6.19	12978	15000	15	13.894	65.21
40/60	930.32	111.11	2.95	60	3.63	12978	15000	15	13.690	65.23
45/55	930.31	111.11	3.08	60	2.82	12978	15000	15	13.751	65.50
50/50	930.28	111.11	3.23	60	3.01	12978	15000	15	13.700	66.81
60/40	930.28	111.11	3.11	60	2.36	12978	15000	15	13.583	66.94
65/35	930.27	111.11	3.25	60	2.17	12978	15000	15	13.335	67.07
70/30	930.27	111.11	3.12	60	1.92	12978	15000	15	13.477	67.12
75/25	930.27	111.11	3.16	60	2.00	12978	15000	15	13.306	67.10

[1] $\bar{v}_c$ is a superficial velocity of the water slug at downstream of micro T-junction, calculated by dividing ($Q_{LCO2} + Q_{H2O}$) over the cross section of the microchannel.

[2] The capillary number calculated by the CO_2 drops.

[3] R_h is the hydrodynamic radius the microchannel, $R_h = (1/2)D_h = (1/2) \cdot 4(WD)/2(W+D) = (WD)/(W+D)$.

[4] The cross section area (A_d) of CO_2 drops is calculated by $A_d = (0.96WD-0.0632W^2)$, see section A.2.

[5] The cross section area (A_c) of water slugs is calculated by $A_c = WD$.

[6] L_t is a nominal total length of the straight channel and $L_t = 15mm$.

[7] L_t' is a real total length of the channel from experiments, the starting point is the back cap of the first generated drop (in a complete plus shape) at position 1 and the ending point is the front cap of the drop that closely approaches to the end of the channel at position 3.

[8] The initial pressure P_0 at the micro T-junction is estimated by the CO_2 pressure that read from the syringe pump.
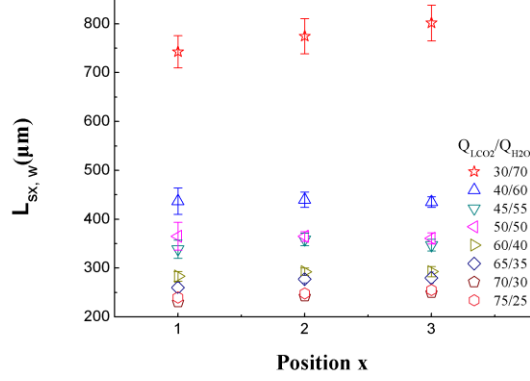
Figure 8. Water slug length at the three positions under various Q_{LCO2}/Q_{H2O}. Each error bar indicates one standard deviation of the mean slug length.
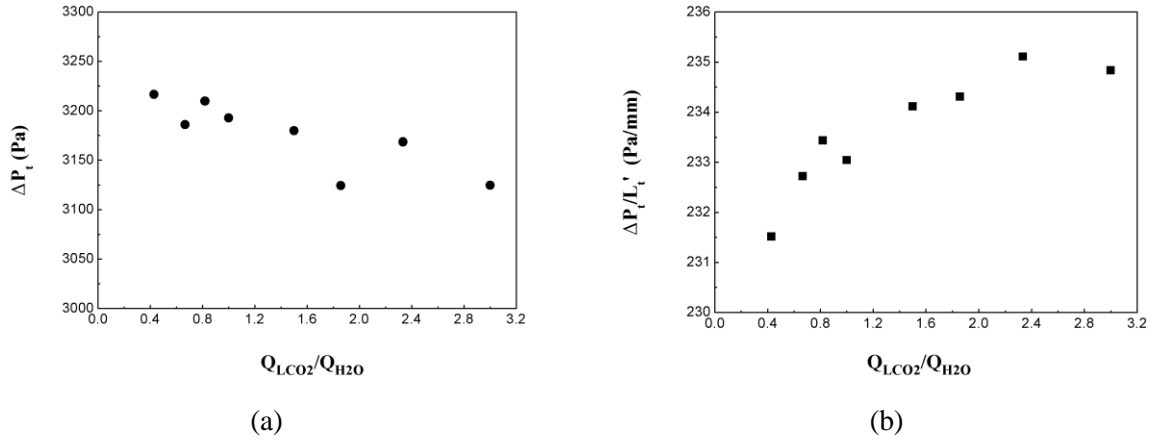

(a)

(b)

Figure 9. (a) Total pressure drops ΔP_t (Pa) over the practical straight microchannel length and (b) pressure drop gradient $\Delta P_t/L_t^{'}$ (Pa/mm, or equivalently, kPa/m), respectively, as a function of flow rate ratio Q_{LCO2}/Q_{H2O}.

As the focus shifts from an absolute pressure drop to a gradient of the pressure drop (i.e., $\Delta P_t/L_t^{'}$), as shown by Figure 9b, smaller length fractions of water slugs (L_c^{*} in Table 1) generally result in a slight increase of $\Delta P_t/L_t^{'}$ as Q_{LCO2}/Q_{H2O} increases from 30/70 to 75/25, though variations are still subtle. This variation tendency reveals that larger occupations of CO_2 drops may lower down overall pressure drops on one hand, but on the other hand, they may lead to a more rapid decline of the pressure drop.

C2. Drop volume change subjected to ΔP_t

Since carbon dioxide (critical temperature $T_c = 304.15$ K and critical pressure $P_c = 7.38$ MPa) is applied as the drop fluid in this study and the temperature during experiments is a room temperature (T = 298.15 K, thus $T_r = T/T_c = 0.98$), equation (29) combined with equation (30) can be specified as

$$P = \frac{RT}{V_m - 2.6659 \times 10^{-5}} - \frac{4.0183 \times 10^{-1}}{V_m^{2} + 5.3318 \times 10^{-5} V_m - 7.107 \times 10^{-10}}, \tag{41}$$

for which R = 8.3145 J/(mol·K) and $\omega = 0.228$ [62,83] of CO_2 are used during the specification. In addition, the equation set (31) can also be rewritten as

17

$$\begin{cases} P_0 = \dfrac{RT}{V_{m0}-2.6659\times10^{-5}} - \dfrac{4.0183\times10^{-1}}{V_{m0}{}^2+5.3318\times10^{-5}V_{m0}-7.107\times10^{-10}}, \\ P_t = \dfrac{RT}{V_{mt}-2.6659\times10^{-5}} - \dfrac{4.0183\times10^{-1}}{V_{mt}{}^2+5.3318\times10^{-5}V_{mt}-7.107\times10^{-10}}, \text{ and} \\ \Delta P_t = P_0 - P_t. \end{cases} \tag{42}$$

Note that V_m, V_{m0} and V_{mt} in the above equation set have a unit of m^3/mol. As argued, an estimated initial pressure (P_0) in addition to the specific pressure decrease is required to evaluate the impact of ΔP_t on drop volume change. It is noted in Table 1 that this initial pressure P_0 at the micro T-junction may be estimated by the CO_2 pressure that reads from the syringe pump, provided that CO_2 under the investigated condition is characterized with much lower viscosities (58.759 ± 0.114) $\mu Pa\cdot s$ compared with water and a much lower flow resistance can result from the pump to the micro T-junction. Estimated initial pressures at the T-junction for all flow conditions are listed in Table 1. By solving the two cubic equations in equation set (42) based on P_0 and P_t, V_{m0} and V_{mt} of CO_2 at position 1 and 3 can be determined, during which only real and rational (specifically, verified by the calculated densities by dividing molar masses over molar volumes) solutions are employed. Figure 10a shows the calculated V_{m0} and V_{mt} with a unit 'ml/mol' (10^{-6} m^3/mol). As Q_{LCO2}/Q_{H2O} increases, the initial pressures P_0 has also been slightly increased from 65.2×10^5 Pa to 67.1×10^5 Pa. Consequently, V_{m0} shows an overall decline, although subtly, from 69.41 ml/mol to 67.59 ml/mol. An almost same tendency arises for V_{mt}. Due to ΔP_t (presented in Figure 9a), P_t always has a slightly smaller ($\sim$3.175 kPa) value than P_0. The difference between P_t and P_0 leads to a very small increase from V_{m0} to V_{mt} by 0.03 ml/mol. According to equation (32), relative drop volumes changes ($\Delta V/V_0$) subjected to ΔP_t can be determined via approximating to $[(V_{mt}/V_{m0}) - 1]$. $\Delta V/V_0$ (scaled by 1000) have been plotted in Figure 10b. It shows that relative drop volumes changes due to the pressure drop are extremely small (approximately 0.39‰ to 0.52‰).
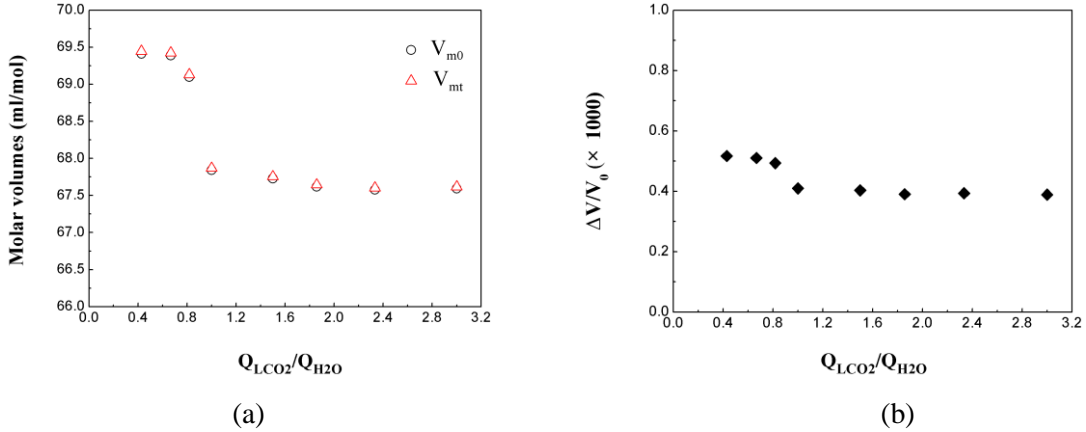

(a)

(b)

Figure 10. (a) Calculated molar volume V_{m0} (ml/mol) and V_{mt} (ml/mol) based on P_0 (see Table 1) and ΔP_t (Figure 9a). (b) Relative drop volume changes $\Delta V/V_0$ (scaled by 1000) calculated from equation (32).

The relative drop length increases $\Delta L'/L_0$ as a result of volume expansions could be equivalent to $\Delta V/V_0$ based on an assumption that the drops, despite volume changes, still maintains a constant cross-sectional area. It should be noted that $\Delta L'$ and L_0 herein are not pertinent to the real drop, but instead, are equivalent ones to ΔL and L_1 (see Figure 9) by accounting for a cylindrical body of the drop. Therefore, $\Delta L'/L_0$ may have same magnitudes as $\Delta V/V_0$ does, which then can be compared to $\Delta L/L_1$ in Figure 9. Clearly, relative drop length reductions ($\Delta L/L_1$) dedicated to the dissolution-diffusion of CO_2 in water are almost two orders of magnitude larger than the pressure drop resulted relative drop length expansions. It is thus concluded that the pressure drop due to the flow resistance of water and the existence of CO_2 Taylor drops in the straight channel does not lead to a significant drop size change, especially when this size change is compared with the shrinkage caused by the interfacial dissolution-diffusion of CO_2 in water.

D. Surface-volume ratios of drops

Surface-to-volume ratio is one of the key parameters that controls the mass transfer (particularly the rates) between different substances, especially when it comes to those occurring at interfaces among fluids and/or even solids. In view of the shrinkages of liquid CO_2 Taylor drops in this study, surface-volume ratios (S/V) of the drops in the microchannel undoubtedly play a key role. According to the formulations of the drop surface area (A) and the drop volume (V), as shown in equation 24 and 25, respectively, these two parameters can be further specified as follows, given that the channel sizes (width W = 150 µm and depth D = 100 µm) are known and a static contact angle θ_c ($\theta_c = 150°$, see figure 5) may be applicable in the hydrodynamic scenarios,

$$A\ (\mu m^2) = 432.2 \cdot L - 522.2, \tag{43}$$

and

$$V\ (\mu m^3) = 12978 \cdot L + 99571.27. \tag{44}$$

in which L(µm) is the drop length, and from experiments $L = L_x$ (x = 1, 2 and 3). Therefore, surface-volume ratios (S/V, 1/mm) of the drops at position 1, 2 and 3 can be determined from the following equation

$$S/V\ (1/mm) = \frac{A}{V} \times 10^3 = \frac{432.2 \cdot L - 522.2}{12978 \cdot L + 99571.27} \times 10^3. \tag{45}$$

Substitute the drop length L (the ones shown in Figure 6b) into equation 45, the surface-volume ratio (S/V) at position 1, 2 and 3 at all the investigated flow rate ratios can be calculated, and the calculated values of S/V are shown in Figure 11. For smaller CO_2 drops resulted from lower Q_{LCO2}/Q_{H2O}, their surface-volume ratios are generally slightly smaller than those of the drops produced at higher Q_{LCO2}/Q_{H2O}. This result is opposite to an intuition that smaller drops might generally possess higher S/V. Quantitatively, the determination of S/V should always take into account the surface area and the volume, in which geometrical morphologies of the Taylor drops with respect to microchannels may be necessary. As a specific drop flows from position 1 to position 2 and down to position 3, it experiences a size reduction in terms of length decrease (see Figure 7a), which also results in a certain extent of decrease of the surface-volume ratio. The S/V decrease due to a size reduction are more notable for the smaller drops which have been produced at $Q_{LCO2}/Q_{H2O} < 1$, however, the S/V differences of the drops generated at $Q_{LCO2}/Q_{H2O} > 1$ among at position 1, 2 and 3 are not so obvious, which is attributed to the long drop lengths (see Figure 7) and relative small length reductions (see Figure 9).
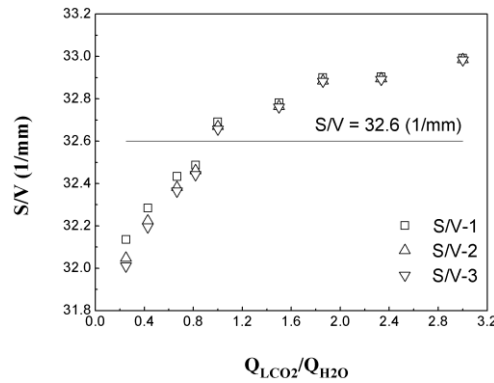

Figure 11. Surface-volume ratios of the CO_2 drops at position 1 (S/V-1, squares), position 2 (S/V-2, up triangles) and position 3 (S/V-3, down triangles), respectively. Horizontal line shows a mean S/V of 32.6 mm^{-1} for all drops.

Despite the S/V difference among various drops produced at Q_{LCO2}/Q_{H2O} ranging from 0.25 to 3, as shown in Figure 11, the S/V of all drops can be averaged at 32.6 ± 0.1 (1/mm). Given that the S/V of all drops are on a

same level (~10^4 m^{-1}), the relative drop length reduction ($\Delta L/L_1$), as shown in Figure 9, are regarded independent of the S/V here in this study.

E. Drop speed and drop flowing time

Equation 26 reveals that the mass transfer between the drop phase and the slug phase is determined by not only the drop length L but also the time scale on which the mass transfer occur. The CO_2 drops certainly take time to travel from position 1 to position 2 and down to position 3; and on the other hand, mass transfer has also been in process within this time period. Therefore, knowledge of the drop speeds in the microchannel from after their generations to the very end of the channel, other than the drop sizes, are required to evaluate the mass transfer. Based on the experimental methodologies discussed in section III.B (shown by equation 35 to 38), the drop speed at position 1 (v-1), position 2 (v-2) and position 3 (v-3) has been measured from the experiment and plotted in Figure 12a against to the corresponding Q_{LCO2}/Q_{H2O}. In addition, a horizontal dash line is added in the figure which shows a constant superficial velocity (v_{Total}) calculated from dividing the constant total flow rates (Q_{LCO2} + Q_{H2O}) over the cross sectional area of the channel, i.e., v_{Total} = (Q_{LCO2} + Q_{H2O})/A. v_{Total} is introduced here for a purpose of comparison with the experimentally measured drop speeds.

When Q_{LCO2}/Q_{H2O} is below 1, all drop speeds at the three positions are lower than v_{Total} (111.1mm/s); however, for one specific flow rate condition, those three drop speeds (i.e., v-1, v-2 and v-3) are very close (differences are less than 3 mm/s) to each other. As can be seen, each drop speed (e.g., v-1) are exactly within the error ranges of the other two speeds (v-2 and v-3). Thus, it is appropriate, in this work, to consider the drop flows as a constant flow speed scenario when Q_{LCO2}/Q_{H2O} is constant and below 1, and an averaged drop speed from the three drop speeds will be applied next for such flow rate conditions (Q_{LCO2}/Q_{H2O} < 1). When Q_{LCO2}/Q_{H2O} > 1, v_{Total} always crosses with all the range lines of the measured drop speeds and separates these error bars nearly into two equivalent parts. It can be interpreted that the measured drop speeds, from wherever the drops are measured, are always in the vicinity of v_{Total}. Besides, focusing on any of all the investigated Q_{LCO2}/Q_{H2O}, it is likely that there exists a decreasing tendency from v-1 to v-2 and down to v-3, which are more notable as the considered Q_{LCO2}/Q_{H2O} is widely larger than 1. Analogous to the cases of Q_{LCO2}/Q_{H2O} < 1, averaged drop speeds based on the measured ones at position 1, 2 and 3 are going to be used to determine the flowing time of drops in the straight channel; note that, however, it does not indicate the flow cases of Q_{LCO2}/Q_{H2O} > 1 are constant drop flows.

Based on averaged drop speeds for each Q_{LCO2}/Q_{H2O} as well as the real channel lengths for the drop flows as shown in Table 1, flowing time of the drops, t$_{flowing}$, in the straight microchannel can be calculated. The averaged drop speed $\bar{v}$ is determined as follows

$$\bar{v} \text{ (mm/s)} = \frac{1}{3}\sum v_x, \text{ x = 1, 2, and 3} \tag{46}$$

and the corresponding standard deviation of $\bar{v}$, $\sigma_{\bar{v}}$, can be calculated based on an error propagation, as shown below,

$$\sigma_{\bar{v}} \text{ (mm/s)} = \sqrt{(\frac{\partial \bar{v}}{\partial v_1})^2 {\sigma_{v_1}}^2 + (\frac{\partial \bar{v}}{\partial v_2})^2 {\sigma_{v_2}}^2 + (\frac{\partial \bar{v}}{\partial v_3})^2 {\sigma_{v_3}}^2}, \tag{47}$$

in which the individual standard deviation σ_{v_x} (x = 1, 2, and 3) has been determined from experimental measurements and been reflected by the error bars in Figure 12a. Consequently, the flowing time of the CO_2 drop in the straight channel is calculated from below

$$t_{flowing} \text{ (ms)} = \frac{L_t'}{\bar{v}} \times 10^3, \tag{48}$$

where L_t' (mm) is the real total channel length for the CO_2 drops and has been introduced in Table 1. Analogously, the uncertainties of $t_{flowing}$ characterized by the standard deviation $\sigma_{t_{flowing}}$ can be quantified as follows

$$\sigma_{t_{flowing}}(ms) = \sqrt{(\frac{\partial t_{flowing}}{\partial \bar{v}})^2 \sigma_{\bar{v}}^2} = 1000 \frac{L_t'}{\bar{v}^2} \sigma_{\bar{v}}. \qquad (49)$$

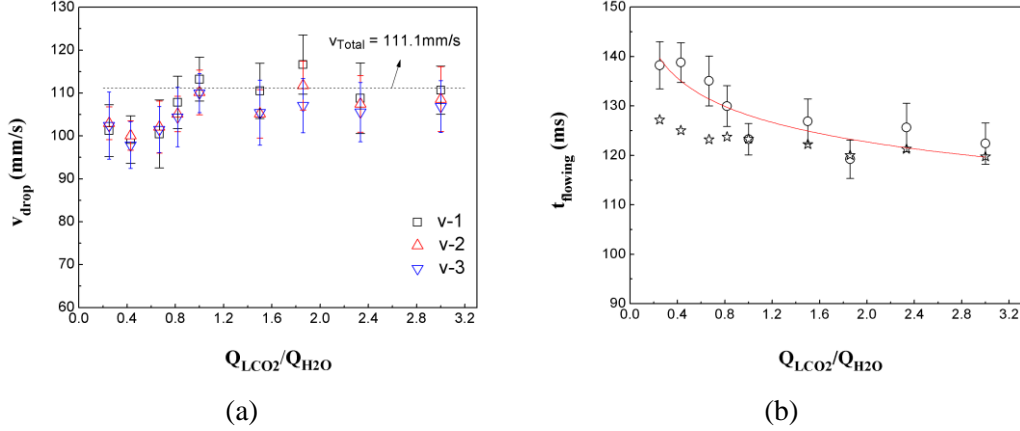(a)   (b)

Figure 12. (a) Liquid CO_2 drop speed at position 1 (v-1, squares), position 2 (v-2, up triangles) and position 3 (v-3, down triangles) under various Q_{LCO2}/Q_{H2O}. A dash line added in the figure shows a superficial total flow velocity from dividing the total flow rate ($Q_{Total} = Q_{LCO2} + Q_{H2O} = 100$ μL/min) over the cross-sectional area ($A = W \cdot D$) of the microchannel. Error bars show one standard deviation for the corresponding drop speed. The error bar caps for v-1, v-2 and v-3 at one specific flow rate ratio are characterized by their widths (the longest for v-1 and the shortest for v-3) for a differentiation purpose. (b) Flowing time ($t_{flowing}$) of CO_2 drops in the straight channel which are respectively determined by equation (48), as shown by the circles, and based on a superficial total flow velocity v_{Total} (111.1 mm/s), as shown by the stars.

According to the above two equations, the flowing time of CO_2 drops are calculated and plotted in Figure 12b. As a reference, the flowing time calculated based on the superficial total flow velocity v_{Total} (111.1 mm/s) are also plotted in Figure 12b. As a consequence of a slight decrease of L_t' from 14mm to 13.3mm, there is a slight decrease of $t_{flowing}$ from 127.2 ms to 120 ms when v_{Total} instead of $\bar{v}$ is applied in equation 48. Apart from L_t', $t_{flowing}$ in Figure 12b (shown by the circles) are subjected to different $\bar{v}$ as well. Generally, the $\bar{v}$ at $Q_{LCO2}/Q_{H2O} < 1$ are marginally smaller than those at $Q_{LCO2}/Q_{H2O} > 1$, as shown by Figure 12a. Consequently, the flowing time $t_{flowing}$ calculated at $Q_{LCO2}/Q_{H2O} < 1$ are approximately 10 ms longer than those calculated at $Q_{LCO2}/Q_{H2O} > 1$, as shown in Figure 12b. Furthermore, as argued previously that $\bar{v}$ may be approximated by v_{Total} when $Q_{LCO2}/Q_{H2O} > 1$, $t_{flowing}$ may also be approximated by those calculated based on v_{Total} for such cases despite a slight difference (no larger than 4%) between the two sets of results. By accounting for the error ranges of the calculated $t_{flowing}$ based on experimentally obtained $\bar{v}$, i.e., the error bars in Figure 12b, a trend line of $t_{flowing}$ from $Q_{LCO2}/Q_{H2O} \sim 0.2$ to $Q_{LCO2}/Q_{H2O} \sim 3$ is added which indicates an inversely proportional development of $t_{flowing}$ as a result of increasing Q_{LCO2}/Q_{H2O}. This trend well justifies the development of the relative total drop length reduction, i.e., $\Delta L/L_1$, as shown in Figure 9, given that the surface-volume ratios S/V for all drops are on a same level (10^4 m^{-1}).

F. Solvent-side mass transfer coefficient k_s

Since the drop length and the flowing time of CO_2 drops in the microchannel are available, as reported in previous sections, the solvent-side mass transfer coefficient (k_s) can thus be determined based equation (26). The channel width (W = 150 μm) and the depth (D = 100 μm) are known. A nominal molar concentration ($C_d = \rho_{CO2}/M$) of pure CO_2, an equilibrium concentration ($C_e \approx 1.27$ mol/L [84,85]) at an assumed sharp interface

(saturated with CO_2 molecules) referred to the pressures listed in table 1, and a constant temperature (T = 298 K) are going to be adopted in our calculations. Moreover, a static contact angle $\theta_c = 150°$ (estimated from Figure 5) between CO_2 drops and water can be applicable as well. Therefore, equation (26) is further specified as follows

$$k_s = 30.03 \frac{c_d}{c_e} (\ln \frac{432.2 L_0 - 522.2}{432.2 L_x - 522.2}) \cdot \frac{1}{t}, \tag{50}$$

in which k_s has a unit of μm/ms, or equivalently, mm/s. In order to determine the nominal molar concentration of CO_2, densities at various initial pressures (P_0 in Table 1) and a constant temperature (298 K) are used, which are referred to the NIST chemistry webbook [86]. Based on the drop length and the drop flowing time reported in Figure 6b and Figure 12b, respectively, we have calculated the mass transfer coefficients $k_{s, 1-3}$, as shown in Figure 13a. It is noted that the $k_{s, 1-3}$ calculated here is a convective mass transport coefficient [87] accounting for a dynamic fluidic scenario within the solvent slug and local convective vortices in the vicinity of the interface with the solute drop. Given with the CO_2 diffusivity ($D_{dc} \approx 1.5 \times 10^{-9}$ m^2/s [82]) in water and that a half channel width as a characteristic length (i.e., $L_{mass} = W/2$) for the mass transfer, the Sherwood number (Sh = $k_{s,1-3}/(D_{dc}/L_{mass})$) that compares the relative strength of the convective mass transfer with that of the purely diffusive one can be determined, the magnitude of which is shown in Figure 13b.

(a)   (b)
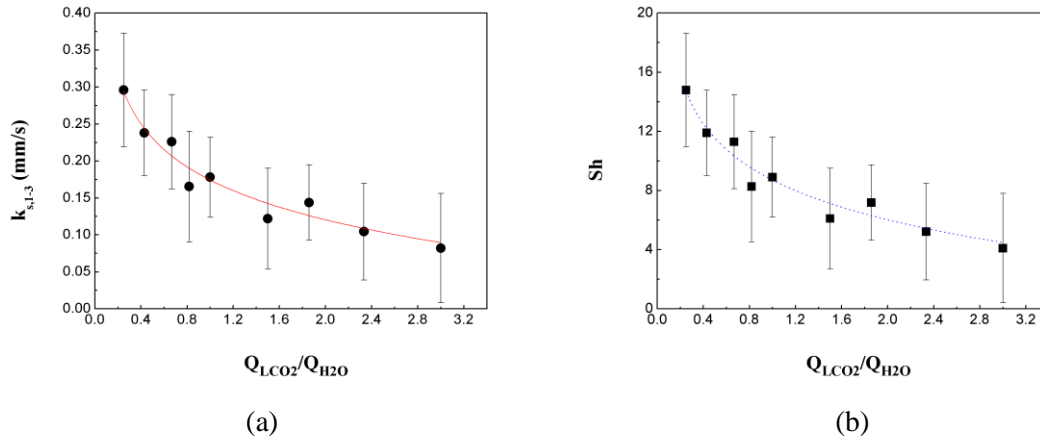
Figure 13. Solvent-side mass transfer coefficients $k_{s,1-3}$ (a) and Sherwood number (b). Error bar indicates the standard deviation calculated according to error propagation.

Figure 13 shows that a slightly larger mass transfer coefficient $k_{s,1-3}$ results at a lower Q_{LCO2}/Q_{H2O} scenario though a longer flowing time and a slightly lower surface-volume ratio exist for a relatively slow drop flow. Despite the variation for $t_{flowing}$ and S/V, these two parameters are generally on the same level among different flow cases. As shown by Figure 7a, the absolute shrinkage of all drops in terms of total length reduction (ΔL) is fairly constant. Further, the absolute drop volume reduction (ΔV) may be constant too in view of a same drop cross section. Back to the Equation (8), the surface area (A) very possibly accounts for the result of $k_{s,1-3}$. For smaller drops produced by lower Q_{LCO2}/Q_{H2O}, they are of smaller surface area but still achieve excellent mass transfer compared with longer ones. In fact, the thin liquid film (thickness ~ 0.02W) close to the channel wall is fluidic stagnant (no flow practically) and could quickly reach saturation when a few solute drops pass by, so it will not contribute to the dissolution anymore in a longer time period and only the front and the back meniscus of each drop are effective regions for the mass transfer. Since the calculation of $k_{s,1-3}$ accounts for the entire surface area, it better reflects the performance of smaller drops and is impaired by the main part of the longer drops that has not contributed much to the mass transfer. Nevertheless, our experimental work reports a solvent-side mass transfer coefficient of 0.1 ~ 0.3 mm/s between water and liquid CO_2 and shows that a smaller size of the solute drop relative to the solvent may be favorable to the mass transport. A similar trend applies to the Sherwood number (Sh) as well provided that D_{dc} and L_{mass} are constants. Revealed by Sh numbers ranging from 4 to 14.8, convections (including local ones on

two sides of the interface and the one in the bulk phase) have dominated over a pure diffusion in controlling the mass transfer. And the relative strength of convection is more profound for the smaller solute drop.

V. Conclusion

In this study, hydrodynamic shrinkage of liquid CO_2 drops in a straight microchannel has been investigated, where the liquid CO_2 takes a form of flowing Taylor drops and water is applied as a continuous solvent phase that behaves as slugs that separate the CO_2 drops. An experimental system introduced in our previous work [78] is utilized in this study. In particular, a micro T-junction with a uniform width (W = 150 µm) and depth (D = 100 µm) fabricated in a silicon/glass microchip is used to produce CO_2 drops, in which liquid CO_2 is injected from a side channel (perpendicular to the main channel) as a dispersed phase and water as a continuous phase flows in the main channel, respectively. As a result of various flow rate ratios (Q_{LCO2}/Q_{H2O}), different CO_2 drops in terms of non-dimensional drop length (L/W) are produced in the micro T-junction. Drop length (L) and drop speed (V) are measured at three specified positions in downstream straight microchannel, namely, position 1 where the drop is exactly pinched off by water, position 2 which is the midpoint of the total length of the straight channel, and position 3 that is located at the very end of the straight channel. Main results are summarized as follows:

◆ Non-dimensional length (L_1/W) of the generated liquid CO_2 drops at the T-junction is correlated with Q_{LCO2}/Q_{H2O}. The correlation is found to be linear but the factor of Q_{LCO2}/Q_{H2O} is much larger than 1 (specifically, 1.79), which is consistent with what we have reported previously [78] that is essentially attributed to the squeezing-elongating effect of the interface during drop generation.

◆ Drop length at position 1 (L_1) to 2 (L_2) and 3 (L_3) shows a decreasing tendency. Detailed drop length reductions are manifested by a total length reduction ΔL ($\Delta L = L_1 - L_3$), a first length reduction ΔL_1 ($\Delta L_1 = L_1 - L_2$), and a second length reduction ΔL_2 ($\Delta L_2 = L_2 - L_3$). All length reductions versus Q_{LCO2}/Q_{H2O} are approximated constant reductions ($\Delta L = (24.35 \pm 1.08)$ µm, $\Delta L_1 = (16.52 \pm 1.71)$ um, $\Delta L_2 = (7.83 \pm 1.17)$ um), which indicates the absolute drop shrinkage may be independent of the original drop size. However, relative length reduction $\Delta L/L_1$ is different among flow rate conditions. $\Delta L/L_1$ decreases from 0.1 to 0.025 as Q_{LCO2}/Q_{H2O} increases from 20/80 to 75/25. Based on formulations of drop surface area and volume, surface-volume ratios (S/V) of all drops at the three positions are determined. Generally, average S/V from at position 1, 2 and 3 shows a declining tendency subjected to increasing Q_{LCO2}/Q_{H2O}. As $Q_{LCO2}/Q_{H2O} > 1$ there is almost no S/V difference among all three position based surface-volume ratios. Overall, S/V for all drops can be averaged at (32.6 ± 0.1) mm^{-1}.

◆ Drop speeds at position 1 (v-1), 2 (v-2) and 3 (v-3) are measured, which are applied to calculate the flowing time ($t_{flowing}$) of CO_2 drops in the channel, and as a further step, the mass transfer coefficient. When $Q_{LCO2}/Q_{H2O} < 1$, these three drop speeds are very close and generally lower than a reference flow velocity v_{Total}, i.e., a superficial velocity by dividing the total flow rate ($Q_{LCO2} + Q_{H2O}$) over the channel cross section. When $Q_{LCO2}/Q_{H2O} > 1$, drop speed decreases from v-1 to v-2 and down to v-3 but still can be approximated by v_{Total}. In order to simplify the calculation of flowing time, an average drop speed ($\bar{v}$) by the three speeds is adopted. Besides, a real channel length instead of the total length dedicated to the drop flow is applied. Due to slightly longer real channel lengths and lower drop speeds, $t_{flowing}$ for $Q_{LCO2}/Q_{H2O} < 1$ are roughly 10 ms longer than those for $Q_{LCO2}/Q_{H2O} > 1$.

◆ Starting from a general form of mass transfer coefficient k_s, a specific form of k_s based on detailed drop surface area and volume by considering microchannel size (width W and depth D), contact angle (θ_c) and drop length L_x (x = 1, 2, 3) has been developed. And by introducing the CO_2 diffusivity and half channel width as a characteristic length, the Sherwood number is determined based on calculated k_s. Generally, lower Q_{LCO2}/Q_{H2O} having produced smaller drops result in slightly higher mass transfer coefficients as well as higher Sh numbers, which is essentially attributed to the larger effective portion of the drop contributing in the mass transfer under

23

same levels of the flowing time $t_{flowing}$, and the S/V for all drops ($\sim 10^4$ m^{-1}). The Sh numbers reveal the dominant roles of convection over pure diffusion in controlling the mass transfer.

◆ Potential effects of the pressure drops (ΔP_t) due to drop flows in the straight microchannel upon the drop volume have been discussed. Despite a slight decrease ($\sim$100 Pa) subjected to increasing Q_{LCO2}/Q_{H2O}, ΔP_t for all conditions is of a mean value of 3175.4 Pa with a standard error of 1.6‰. By inducing the Peng-Robinson EOS [62] and using estimated initial pressures (P_0) at the T-junction (from the CO_2 pump), drop volume changes relative to original ones are correlated to molar volumes in the EOS and are quantified. Resulted volume changes are calculated as small quantities ($\Delta V/V_0$: 0.39‰ $\sim$ 0.52‰).

ACKNOWLEDGEMENT

REFERENCE

[1]   Bird, R.B., Stewart, W.E. & Lightfoot, E.N. (2002). Transport Phenomena (John Wiley & Sons, New York, US, 2002).

[2]   Higbie, R. (1935) The rate of absorption of a pure gas into a still liquid during short periods of exposure. Transactions of the AIChE, 31, 365-389.

[3]   Ward, C. A., & Fang, G. (1999). Expression for predicting liquid evaporation flux: Statistical rate theory approach. Physical Review E, 59(1), 429.

[4]   Handlos, A. E., & Baron, T. (1957). Mass and heat transfer from drops in liquid-liquid extraction. AIChE Journal, 3(1), 127-136.

[5]   Danckwerts, P. V. (1955). Gas absorption accompanied by chemical reaction. AIChE Journal, 1(4), 456-463.

[6]   Olander, D. R. (1960). Simultaneous mass transfer and equilibrium chemical reaction. AIChE Journal, 6(2), 233-239.

[7]   Kashid, M. N., Renken, A., & Kiwi-Minsker, L. (2011). Gas–liquid and liquid–liquid mass transfer in microstructured reactors. Chemical Engineering Science, 66(17), 3876-3897.

[8]   Whitman, W. G. (1923). A preliminary experimental confirmation of the two film theory of gas absorption. Chemical and Metallurgical Engineering, 29, 146-148.

[9]   Kuo, J. S., & Chiu, D. T. (2011). Controlling mass transport in microfluidic devices. Annual Review of Analytical Chemistry, 4, 275-296.

[10]   Perry, R. H., & Green, D. W. (2008). Perry's chemical engineers' handbook. (McGraw-Hill, New York, US, 2008).

[11]   Visscher, F., Van der Schaaf, J., Nijhuis, T. A., & Schouten, J. C. (2013). Rotating reactors-A review. Chemical Engineering Research and Design, 91(10), 1923-1940.

[12]   Klaewkla, R., Arend, M., & Hoelderich, W. F. (2011). A review of mass transfer controlling the reaction rate in heterogeneous catalytic systems (Vol. 5). INTECH Open Access Publisher.

[13]   Löffler, D. G., & Schmidt, L. D. (1977). Influence of external mass transfer on catalytic reaction rates on metals. Industrial & Engineering Chemistry Fundamentals, 16(3), 362-366.

[14]   Angeli, P., & Hewitt, G. F. (2000). Drop size distributions in horizontal oil-water dispersed flows. Chemical Engineering Science, 55(16), 3133-3143.

[15]   Simmons, M. J. H., & Azzopardi, B. J. (2001). Drop size distributions in dispersed liquid–liquid pipe flow. International journal of multiphase flow, 27(5), 843-859.

[16] Lovick, J., & Angeli, P. (2004). Droplet size and velocity profiles in liquid–liquid horizontal flows. Chemical engineering science, 59(15), 3105-3115.

[17] Umbanhowar, P. B., Prasad, V., & Weitz, D. A. (2000). Monodisperse emulsion generation via drop break off in a coflowing stream. Langmuir, 16(2), 347-351.

[18] Ganan-Calvo, A.M., Gordillo, J.M., (2001). Perfectly monodisperse microbubbling by capillary flow focusing. Physical Review Letters 87, 2745011–2745014.

[19] Garstecki, P., Gitlin, I., DiLuzio, W., Whitesides, G. M., Kumacheva, E., & Stone, H. A. (2004). Formation of monodisperse bubbles in a microfluidic flow-focusing device. Applied Physics Letters, 85(13), 2649-2651.

[20] Anna, S. L., Bontoux, N., & Stone, H. A. (2003). Formation of dispersions using "flow focusing" in microchannels. Applied physics letters, 82(3), 364-366.

[21] Rodríguez-Rodríguez, J., Sevilla, A., Martínez-Bazán, C., & Gordillo, J. M. (2015). Generation of microbubbles with applications to industry and medicine. Annual Review of Fluid Mechanics, 47, 405-429.

[22] Stone, H. A., Stroock, A. D., & Ajdari, A. (2004). Engineering flows in small devices: microfluidics toward a lab-on-a-chip. Annu. Rev. Fluid Mech., 36, 381-411.

[23] Suh, Y. K., & Kang, S. (2010). A review on mixing in microfluidics. Micromachines, 1(3), 82-111.

[24] Au, A. K., Huynh, W., Horowitz, L. F., & Folch, A. (2016). 3D-Printed Microfluidics. Angewandte Chemie International Edition, 55, 3862-3881.

[25] Demello, A. J. (2006). Control and detection of chemical reactions in microfluidic systems. Nature, 442(7101), 394-402.

[26] McMullen, J. P., & Jensen, K. F. (2011). Rapid determination of reaction kinetics with an automated microfluidic system. Organic Process Research & Development, 15(2), 398-407.

[27] Riechers, B., Maes, F., Akoury, E., Semin, B., Gruner, P., & Baret, J. C. (2016). Surfactant adsorption kinetics in microfluidics. Proceedings of the National Academy of Sciences, 113(41), 11465-11470.

[28] Kashid, M.N., Kiwi-Minsker, L., 2009. Microstructured reactors for multiphase reactions: state of the art. Industrial & Engineering Chemistry Research 48, 6465–6485.

[29] van Baten, J.M., Krishna, R., 2004. CFD simulations of mass transfer from Taylor bubbles rising in circular capillaries. Chemical Engineering Science 59, 2535–2545.

[30] Yue, J., Chen, G., Yuan, Q., Luo, L., Gonthier, Y., 2007. Hydrodynamics and mass transfer characteristics in gas–liquid flow through a rectangular microchannel. Chemical Engineering Science 62, 2096–2108.

[31] Sobieszuk, P., Pohorecki, R., Cygański, P., & Grzelka, J. (2011). Determination of the interfacial area and mass transfer coefficients in the Taylor gas–liquid flow in a microchannel. Chemical Engineering Science, 66(23), 6048-6056.

[32] Tan, J., Lu, Y. C., Xu, J. H., & Luo, G. S. (2012). Mass transfer performance of gas–liquid segmented flow in microchannels. Chemical Engineering Journal, 181, 229-235.

[33] Kastens, S., Hosoda, S., Schlüter, M., & Tomiyama, A. (2015). Mass transfer from single Taylor bubbles in minichannels. Chemical Engineering & Technology, 38(11), 1925-1932.

[34] Abolhasani, M., Kumacheva, E., & Günther, A. (2015). Peclet Number Dependence of Mass Transfer in Microscale Segmented Gas–Liquid Flow. Industrial & Engineering Chemistry Research, 54(36), 9046-9051.

[35] Burns, J. R., & Ramshaw, C. (2001). The intensification of rapid reactions in multiphase systems using slug flow in capillaries. Lab on a Chip, 1(1), 10-15.

[36] Kashid, M. N., Gerlach, I., Goetz, S., Franzke, J., Acker, J. F., Platte, F., Agar, D.W., & Turek, S. (2005). Internal circulation within the liquid slugs of a liquid-liquid slug-flow capillary microreactor. Industrial & Engineering Chemistry Research, 44(14), 5003-5010.

[37] Kashid, M. N., Harshe, Y. M., & Agar, D. W. (2007). Liquid-liquid slug flow in a capillary: An alternative to suspended drop or film contactors. Industrial & Engineering Chemistry Research, 46(25), 8420-8430.

[38] Xu, B., Cai, W., Liu, X., & Zhang, X. (2013). Mass transfer behavior of liquid–liquid slug flow in circular cross-section microchannel. Chemical Engineering Research and Design, 91(7), 1203-1211.

[39] Raimondi, N. D. M., Prat, L., Gourdon, C., & Tasselli, J. (2014). Experiments of mass transfer with liquid–liquid slug flow in square microchannels. Chemical Engineering Science, 105, 169-178.

[40] Tsaoulidis, D., & Angeli, P. (2015). Effect of channel size on mass transfer during liquid–liquid plug flow in small scale extractors. Chemical Engineering Journal, 262, 785-793.

[41] Hassan, I., Vaillancourt, M., Pehlivan, K. (2005). Two-phase flow regime transitions in microchannels: a comparative experimental study. Microscale Thermophysical Engineering 9, 165–182.

[42] Kashid, M.N., Renken, A., Kiwi-Minsker, L. (2011). Influence of flow regime on mass transfer in different types of microchannels. Industrial & Engineering Chemistry Research 50 (11), 6906–6914.

[43] Seemann, R., Brinkmann, M., Pfohl, T., & Herminghaus, S. (2011). Droplet based microfluidics. Reports on Progress in Physics, 75(1), 016601.

[44] Nunes, J. K., Tsai, S. S. H., Wan, J., & Stone, H. A. (2013). Dripping and jetting in microfluidic multiphase flows applied to particle and fibre synthesis. Journal of Physics D: Applied physics, 46(11), 114002.

[45] Ito, Y., & Komori, S. (2008). Mass transfer across gas-liquid interface in a capillary tube. Journal of Chemical Engineering of Japan, 41(10), 947-952.

[46] Angeli, P., & Gavriilidis, A. (2008). Hydrodynamics of Taylor flow in small channels: a review. Proceedings of the Institution of Mechanical Engineers, Part C: Journal of Mechanical Engineering Science, 222(5), 737-751.

[47] Bercic, G., & Pintar, A. (1997). The role of gas bubbles and liquid slug lengths on mass transport in the Taylor flow through capillaries. Chemical Engineering Science, 52, 3709–3719.

[48] Taylor, G. I. Deposition of a viscous fluid on the wall of a tube. (1961). Journal of Fluid Mechanics, 10, 161–165.

[49] Gunther, A., Khan, S.A., Thalmann, M., Trachsel, F., & Jensen, K.F. (2004). Transport and reaction in micro scale segmented gas–liquid flow. Lab on a Chip, 4(4), 278–286.

[50] Kinoshita, H., Kaneda, S., Fujii, T., & Oshima, M. (2007). Three-dimensional measurement and visualization of internal flow of a moving droplet using confocal micro-PIV. Lab on a Chip, 7(3), 338-346.

[51] Abolhasani, M., Günther, A., & Kumacheva, E. (2014). Microfluidic studies of carbon dioxide. *Angewandte Chemie International Edition*, *53*(31), 7992-8002.

[52] Working group III of the Intergovernmental Panel on Climate Change [Metz, B., O. Davidson, H. C. de Coninck, M. Loos, and L. A. Meyer (eds.)]. (2005). IPCC special report on carbon dioxide capture and storage. (Cambridge University Press, Cambridge, United Kingdom, 2005).

[53] Leitner, W. (2002). Supercritical carbon dioxide as a green reaction medium for catalysis. Accounts of Chemical Research, 35(9), 746-756.

[54] Licence, P., Ke, J., Sokolova, M., Ross, S. K., & Poliakoff, M. (2003). Chemical reactions in supercritical carbon dioxide: from laboratory to commercial plant. Green Chemistry, 5(2), 99-104.

[55] Sun, R., & Cubaud, T. (2011). Dissolution of carbon dioxide bubbles and microfluidic multiphase flows. Lab on a Chip, 11(17), 2924-2928.

[56] Cubaud, T., Sauzade, M., & Sun, R. (2012). CO_2 dissolution in water using long serpentine microchannels. Biomicrofluidics, 6(2), 022002.

[57] Tumarkin, E., Nie, Z., Park, J. I., Abolhasani, M., Greener, J., Sherwood-Lollar, B, Gunther A., Kumacheva, E. (2011). Temperature-controlled 'breathing' of carbon dioxide bubbles. Lab on a Chip, 11(20), 3545-3550.

[58] Abolhasani, M., Singh, M., Kumacheva, E., Günther, A. (2012). Automated microfluidic platform for studies of carbon dioxide dissolution and solubility in physical solvents. Lab on a Chip, 12(9), 1611-1618.

[59] Lefortier, S. G., Hamersma, P. J., Bardow, A., & Kreutzer, M. T. (2012). Rapid microfluidic screening of CO_2 solubility and diffusion in pure and mixed solvents. Lab on a Chip, 12(18), 3387-3391.

[60] Shim, S., Wan, J., Hilgenfeldt, S., Panchal, P. D., & Stone, H. A. (2014). Dissolution without disappearing: multicomponent gas exchange for CO_2 bubbles in a microfluidic channel. Lab on a Chip, 14(14), 2428-2436.

[61] Zhu, C., Li, C., Gao, X., Ma, Y., & Liu, D. (2014). Taylor flow and mass transfer of CO_2 chemical absorption into MEA aqueous solutions in a T-junction microchannel. International Journal of Heat and Mass Transfer, 73, 492-499.

[62] Peng, D., & Robinson D.B. (1976). A new two-constant equation of state. Industrial & Engineering Chemistry Fundamentals, 15(1), 59-64.

[63] Dore, V., Tsaoulidis, D., & Angeli, P. (2012). Mixing patterns in water plugs during water/ionic liquid segmented flow in microchannels. Chemical Engineering Science, 80, 334-341.

[64] http://www.numericana.com/answer/ellipsoid.htm, accessed on November 11, 2016.

[65] Kolb, W. B., & Cerro, R. L. (1993). Film flow in the space between a circular bubble and a square tube. Journal of Colloid And Interface Science, 159(2), 302-311.

[66] Fries, D. M., Trachsel, F., & von Rohr, P. R. (2008). Segmented gas–liquid flow characterization in rectangular microchannels. International Journal of Multiphase Flow, 34(12), 1108-1118.

[67] Eain, M. M. G., Egan, V., Howard, J., Walsh, P., Walsh, E., & Punch, J. (2015). Review and extension of pressure drop models applied to Taylor flow regimes. International Journal of Multiphase Flow, 68, 1-9.

[68] Warnier, M. J. F., De Croon, M. H. J. M., Rebrov, E. V., & Schouten, J. C. (2010). Pressure drop of gas–liquid Taylor flow in round micro-capillaries for low to intermediate Reynolds numbers. Microfluidics and Nanofluidics, 8(1), 33-45.

[69] Bretherton, F. P. (1961). The motion of long bubbles in tubes. Journal of Fluid Mechanics, 10(2), 166-188.

[70] Aussillous, P., & Quéré, D. (2000). Quick deposition of a fluid on the wall of a tube. Physics of Fluids,12(10), 2367-2371.

[71] Van Der Waals, J. D., & Rowlinson, J. S. (1988). J.D. van der Waals : on the continuity of the gaseous and liquid states. (North-Holland, Amsterdam, Netherlands, 1988).

[72] Redlich, O., & Kwong, J. N. (1949). On the thermodynamics of solutions. V. An equation of state. Fugacities of gaseous solutions. Chemical reviews, 44(1), 233-244.

[73] Soave, G. (1972). Equilibrium constants from a modified Redlich-Kwong equation of state. Chemical Engineering Science, 27(6), 1197-1203.

[74] Martin, J. J. (1979). Cubic equations of state-which?. Industrial & Engineering Chemistry Fundamentals, 18(2), 81-97.

[75] Péneloux, A., Rauzy, E., & Fréze, R. (1982). A consistent correction for Redlich-Kwong-Soave volumes. Fluid phase equilibria, 8(1), 7-23.

[76] Patel, N. C., & Teja, A. S. (1982). A new cubic equation of state for fluids and fluid mixtures. Chemical Engineering Science, 37(3), 463-473.

[77] Valderrama, J. O. (2003). The state of the cubic equations of state. Industrial & Engineering Chemistry Research, 42(8), 1603-1618.

[78] Qin, N., Wen, J. Z., & Ren, C. L. (2017). Highly pressurized partially miscible liquid-liquid flow in a micro-T-junction. I. Experimental observations. Physical Review E, 95(4), 043110.

[79] Lide, D. R. (2005). CRC Handbook of Chemistry and Physics (CRC Press, Boca Raton, Florida, US, 2005).

[80] Hebach, A., Oberhof, A., Dahmen, N., Kögel, A., Ederer, H., & Dinjus, E. (2002). Interfacial tension at elevated pressures measurements and correlations in the water+ carbon dioxide system. Journal of Chemical & Engineering Data, 47(6), 1540-1546.

[81] Georgiadis, A., Maitland, G., Trusler, J. M., & Bismarck, A. (2010). Interfacial tension measurements of the (H_2O + CO_2) system at elevated pressures and temperatures. Journal of Chemical & Engineering Data, 55(10), 4168-4175.

[82] Qin, N., Wen, J. Z., & Ren, C. L. (2017). Highly pressurized partially miscible liquid-liquid flow in a micro-T-junction. II. Theoretical justifications and modeling. Physical Review E, 95(4), 043111.

[83] Martynov, S., Brown, S., & Mahgerefteh, H. (2013). An extended Peng-Robinson equation of state for carbon dioxide solid-vapor equilibrium. Greenhouse Gases: Science and Technology, 3(2), 136-147.

[84] Spycher, N., Pruess, K., & Ennis-King, J. (2003). CO_2-H_2O mixtures in the geological sequestration of CO 2. I. Assessment and calculation of mutual solubilities from 12 to 100 C and up to 600 bar. Geochimica et cosmochimica acta, 67(16), 3015-3031.

[85] Diamond, L. W., & Akinfiev, N. N. (2003). Solubility of CO_2 in water from-1.5 to 100℃ and from 0.1 to 100 MPa: evaluation of literature data and thermodynamic modelling. Fluid phase equilibria, 208(1), 265-290.

[86] http://webbook.nist.gov/chemistry/fluid/, accessed on December 21, 2016.

[87] Welty, J. R., Wicks, C. E., Rorrer, G., & Wilson, R. E. (2009). Fundamentals of momentum, heat, and mass transfer (John Wiley & Sons, Inc., New York, US., 2009).